Pergamon

PII S0016-7037(02)00912-2

Structures of quartz (10$\bar{1}$0)- and (10$\bar{1}$1)-water interfaces determined by X-ray reflectivity and atomic force microscopy of natural growth surfaces

Michel L. Schlegel,[1,†] Kathryn L. Nagy,[1,*] Paul Fenter[2] and Neil C. Sturchio[3]

[1]Department of Geological Sciences, University of Colorado, 399 UCB, Boulder, CO 80309, USA
[2]Environmental Research Division, Argonne National Laboratory, Argonne, IL 60439, USA
[3]Department of Earth and Environmental Sciences, University of Illinois at Chicago, Chicago, IL 60607, USA

Abstract—The structures of prismatic (10$\bar{1}$0) and pyramidal (10$\bar{1}$1) growth faces of natural quartz crystals, and their modification upon annealing at T ≤ 400°C were investigated ex situ by atomic force microscopy (AFM) and in water by high-resolution X-ray reflectivity. AFM images revealed the presence of ∼ 0.1 to 1 μm-wide flat terraces delimited by steps of one to several unit cells in height. These steps follow approximately directions given by the intersection of growth faces. Modeling of X-ray reflectivity data indicates that surface silica groups on flat terraces have only one free Si-O bond each (presumably hydroxylated), except for some having two free Si-O bonds observed on a single (10$\bar{1}$0) surface. Vertical relaxation of atomic positions (< 0.4 Å for terminal oxygens and < 0.2 Å for silicon and oxygen atoms fully coordinated to structural tetrahedra) is limited to a depth of 14 Å. Electron density profiles for all measured interfaces are consistent with a single layer of adsorbed water, with no evidence for additional organization of water molecules into distinct layers extending into the bulk solution. Similar interfacial structures were observed for natural and annealed surfaces of identical crystallographic orientation, indicating that extensive reconstruction of the silica network at the quartz surface did not occur under the annealing conditions. *Copyright © 2002 Elsevier Science Ltd*

1. INTRODUCTION

Quartz is ubiquitous in Earth's continental crust (MacDonald, 1983; Heaney, 1996), and plays a key role in the geochemistry of aqueous systems (Schulz and White, 1999). For example, concentrations of silicic acid in low-temperature terrestrial waters typically range from 10 to 80 ppm (Davies and De Wiest, 1966), the lower end of which is controlled by quartz solubility (∼ 11 ppm; Rimstidt, 1997). Thorough characterization of quartz dissolution and precipitation kinetics is therefore central to understanding the cycling of dissolved silica (Dove, 1995). Furthermore, both natural observations and experimental studies have shown that ferrous or aluminous coatings (Morris and Fletcher, 1987; Coston et al., 1995; Davis et al., 1998), and layered silicates (Manceau et al., 1999) can form on quartz grains at surface temperatures. Dissolution and sorption properties of quartz have been investigated (Henderson et al., 1970; Kamiya and Shimokata, 1976; Rimstidt and Barnes, 1980; Brantley et al., 1986; Schwarzentruber et al., 1987; Knauss and Wolery, 1988; Brady and Walther, 1989; Brady and Walther, 1990; Dove and Crerar, 1990; Dove and Elston, 1992; Berger et al., 1994; Dove, 1994; Tester et al., 1994; O'Day et al., 1996; Dove and Nix, 1997; Gautier et al., 2001), and results of these solution chemistry experiments interpreted using surface complexation kinetic and equilibrium models (Hiemstra and Van Riemsdijk, 1990; Dove, 1994; Tester et al., 1994; Dove and Nix, 1997; Schulz and White, 1999). However, the validity of these surface chemistry models

and full characterization of reaction kinetics hinge on a detailed knowledge of the structural and energetic properties of the quartz-water interface, such as the topography of the mineral surface (Lasaga, 1990), the nature, concentration and structure of reactive sites (Hiemstra and Van Riemsdijk, 1990; Koretsky et al., 1998), and the properties of interfacial water (Du et al., 1994). The kinetics of surface reactions, however, have been related thus far to morphologic and structural properties of the quartz surface in only a few studies (Brantley et al., 1986; Gratz et al., 1990; Gratz et al., 1991; Gratz and Bird, 1993a; Gautier et al., 2001).

The surface relaxation and reconstruction of silica minerals, as well as the interaction of their surface functional groups with water and ions, have been extensively explored by first principles methods (Geerlings et al., 1984; Lasaga, 1990; Lasaga and Gibbs, 1990; Ugliendo et al., 1990; Kubicki et al., 1993; Xiao and Lasaga, 1996; De Leeuw et al., 1999; Koudriachova et al., 2001). Rapid interaction of silicon dangling bonds with water molecules and formation of silanol surface groups, in which a hydroxylated oxygen is bound to only one silicon atom, were predicted by ab initio methods (De Leeuw et al., 1999) and by application of bond valence theory (Brown, 1992; Hiemstra et al., 1996; Koretsky et al., 1998), and also were observed experimentally by infrared (IR) spectroscopy (Gallei and Parks, 1972; Morrow and Cody, 1976; Koretsky et al., 1997). Silanol groups were inferred to form hydrogen bridges with adsorbed water molecules (Ugliendo et al., 1990). This type of interaction would result in a net orientation of the negatively charged end of the water dipole toward the surface, which was observed by sum frequency generation spectroscopy at the point of zero charge (Du et al., 1994). Highly strained siloxane bonds (between one oxygen and two silicons) were also inferred to hydrolyze easily and form silanol groups (Heggie and Jones,

* Author to whom correspondence should be addressed (kathryn.nagy@colorado.edu).
† *Present address:* CEA de Saclay, DPC/SCPA/LCRE, Bât. 450 - BP 11, F-91191 Gif-sur-Yvette Cedex-France

1987). Further minimization of surface energy may occur by relaxation and reconstruction of the quartz surface. Both ab initio calculations (De Leeuw et al., 1999) and low energy electron diffraction (LEED) data obtained under high vacuum conditions (Bart et al., 1992; Bart and Gautier, 1994; Bart et al., 1994) suggest that surface relaxation is limited.

To assess these theoretical and spectroscopic results, direct determination of the structural properties of the quartz-water interface including relaxation is warranted. Such structural characterization may be obtained using in-situ high-resolution X-ray reflectivity (Sturchio et al., 1997; Fenter and Sturchio, 1999; Fenter et al., 2000a, 2000b; Cheng et al., 2001; Eng et al., 2001). X-ray reflectivity relies on scattering of X-rays at the mineral-water interface. The weak reflectivity signal is directly related to the electron density profile across this interface, and thus permits the identification of surface properties such as the extent of solid relaxation, the presence of adsorbed layers of molecules (Robinson, 1986; Feidenhans'l, 1989; Fenter and Sturchio, 1999; Fenter et al., 2000a, 2000b), and the structure of interfacial water (Cheng et al., 2001). X-ray reflectivity requires atomically flat surfaces, which for quartz may be obtained from growth faces of gem-quality crystals (Gratz et al., 1990; Gratz et al., 1991). Reflectivity measurements can be complemented by atomic force microscopy (AFM) to determine surface topographic features of quartz at the molecular scale.

Our work provides a quantitative determination of the structural properties of the quartz-water interface for two natural growth surfaces. Surface topography and roughness on untreated crystals and crystals annealed at moderate temperatures (300 to 400°C) were assessed ex situ by AFM and in situ by X-ray reflectivity. The identity of surface terminations, magnitude of atomic-scale structural relaxations, and structure of water near these quartz surfaces were determined from reflectivity data.

2. THE X-RAY REFLECTIVITY TECHNIQUE

In an X-ray reflectivity experiment, the ratio of the reflected to the incident X-ray flux (i.e., the reflectivity, $R(Q)$) at an interface between two phases is measured as a function of the momentum transfer $Q = (4\pi/\lambda)\sin(\theta)$, where θ is the angle between the incident X-ray beam and the surface plane, and λ is the X-ray wavelength. The X-ray reflectivity is related to the laterally-averaged electron density profile, $\rho(z)$, close to a reflecting interface by

$$R(Q) = (4\pi r_e/QA_{hkl})^2 \left| \int \rho(z)e^{iQz}\,dz \right|^2, \qquad (1)$$

where $r_e = 2.818 \times 10^{-5}$ Å is the classical electron radius, z is the height with respect to the interface, and A_{hkl} is the two-dimensional area of the unit cell in the (hkl) plane (Robinson and Tweet, 1992). $R(Q)$ can vary over several orders of magnitude, from values ~ 1 at the Bragg conditions, to values $\leq 10^{-10}$. The small reflectivity values between bulk Bragg peaks are sensitive to the nature of the surface terminations and to modifications of electron density profiles resulting from changes in the atomic structure at the mineral-water interface (Robinson and Tweet, 1992). When these measurements are made at high (~ 1 Å) resolution, reflectivity data are sensitive to the atomic arrangements at the mineral surface. This sensitivity allows determination of the structural properties of the mineral-water interface (such as atomic relaxation and the adsorption of water and ions). For this purpose, $R(Q)$ can be recast in terms of X-ray scattering by atoms as

$$R(Q) = B(Q) \cdot (4\pi r_e/QA_{hkl})^2 \left| \sum_j f_j \exp(iQz_j)\exp[-(Qu_j)^2] \right|^2,$$
$$(2)$$

where f_j, z_j and u_j are the atomic scattering factor, the height, and the Debye-Waller parameter summed laterally over all atoms that are within the surface unit cell and vertically over all atoms in the substrate crystal, the surface region, and the fluid layer above the surface. $B(Q)$ accounts for changes in the reflected intensity due to surface roughness in the form of steps. Distinct analytical models may account for $B(Q)$ according to the nature of surface roughness. In the present paper, surface roughness is shown to result mainly from the presence of unit-cell high steps separating terraces that are flat at the scale of vertical resolution (≤ 1 Å) of the AFM over laterally-averaged areas of a few or more square nanometers. If we assume that the total area of any partial layer or terrace can be expressed as a fraction β ($0 \leq \beta < 1$) of the total area of the underlying layer, then $B(Q)$ can be written as (Robinson, 1986)

$$B(Q) = (1 - \beta^2)/[1 + \beta^2 - 2\beta\cos(Q^*d_{hkl})], \qquad (3)$$

where d_{hkl} is the spacing between Bragg planes parallel to the surface and β is related to the root-mean-square surface roughness (σ_{rms}) by (Robinson, 1986)

$$\sigma_{rms} = \frac{\sqrt{\beta}}{1 - \beta} d_{hkl}. \qquad (4)$$

The relationship in Eqn. 2 makes it possible to test and optimize interfacial structural models quantitatively by least-squares fits to reflectivity data (Feidenhans'l, 1989). Such models are built by starting with the bulk crystal structure, cleaving the crystal along a surface parallel to the crystallographic plane of interest, allowing for relaxation of individual atom positions near the surface, and completing the interface with a physically reasonable model for interfacial and bulk water (Fenter et al., 2000a, 2000b). The starting "unrelaxed" positions of interfacial atoms are obtained from the crystal structure which, for quartz, can be viewed as trigonal tunnels formed by spiraling chains of corner-linked silicon tetrahedra (Fig. 1a). The primitive {$\mathbf{a}$, $\mathbf{b}$, $\mathbf{c}$} crystallographic cell for this crystal structure is rhombohedral, but usually a non-primitive hexagonal cell with a threefold screw symmetry axis is referenced. There are two different possible settings for the basis of these lattices, either obverse {$\mathbf{a_1}$, $\mathbf{a_2}$, $\mathbf{a_3}$, $\mathbf{c_1}$} ($\mathbf{a_3} = -\mathbf{a_1} - \mathbf{a_2}$) or reverse {$\mathbf{a'_1}$, $\mathbf{a'_2}$, $\mathbf{a'_3}$, $\mathbf{c_1}$}, the latter being obtained by rotating the former by $\pi/3$ around $\mathbf{c_1}$ (Fig. 1b; Boisen and Gibbs, 1990; Heaney, 1996). As a result, an {hkl̄l} crystallographic plane in the obverse setting coincides with the {h̄k̄l̄l} plane in the reverse setting. Here, we notate the surface orientations using the obverse setting.
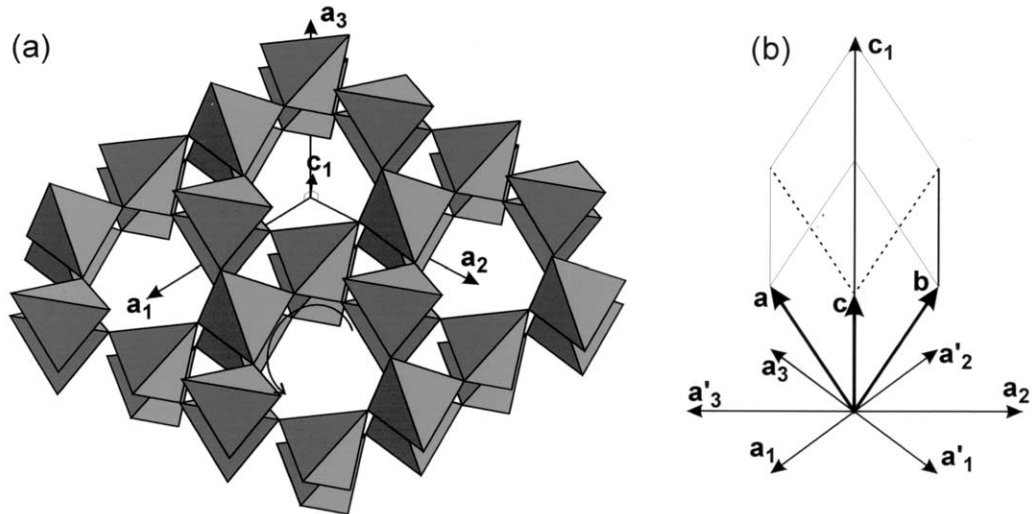
Fig. 1. (a) Polyhedral representation of the quartz structure. Silicon tetrahedra share corners and form spirals of trigonal symmetry. $\{a_1, a_2, a_3, c_1\}$ is the non-primitive hexagonal cell in the obverse setting (Heaney, 1996). (b) Comparison of the primitive $\{a, b, c\}$ crystallographic cell with the two possible hexagonal cells $\{a_1, a_2, a_3, c_1\}$ or $\{a'_1, a'_2, a'_3, c_1\}$.

3. MATERIALS AND METHODS

3.1. Quartz Origin and Preparation

Natural growth surfaces of $(10\bar{1}0)$ ("prismatic") and $(10\bar{1}1)$ ("pyramidal") orientation from optically-clear, doubly-terminated crystals (Herkimer "diamonds," Herkimer County, New York) were used for this study. Optically-flat surfaces were selected under a binocular microscope, and recovered as ~ 1 mm-thick slabs with a diamond wafering saw. Surfaces were ultrasonically cleaned 15 min in methanol and 15 min in deionized water, and then dried under an Ar stream, except for one $(10\bar{1}1)$ surface which was kept in deionized water for 10 months before X-ray reflectivity measurements. These are referred to as "natural" surfaces. Some slabs were further annealed in air, either at 300°C for 50 h [$(10\bar{1}0)$ surface] or at 400°C for 48 h [$(10\bar{1}1)$ surface]. All slabs were then stored in closed petri dishes under ambient atmosphere.

3.2. Atomic Force Microscopy

Quartz slabs were cleaned ultrasonically for 15 min in high purity acetone (Fisher, Optima grade), 15 min in methanol, and 15 min in deionized water, to remove hydrophobic, amphiphilic (e.g., fatty acids) and hydrophilic surface contaminants, respectively. A final 15 min sonication in acetone was followed by drying in air. The slabs were then mounted on steel disks using double-sided adhesive tape. TappingMode AFM (TMAFM) images were collected in air at scanning rates ≤ 0.7 Hz, using a Digital Instruments Nanoscope IIIa MultiMode scanning probe microscope and silicon tips (Nanoscope SESPW). Four to ten 4×4 μm areas were imaged on each crystal to assess lateral uniformity of the surface. All images were analyzed for step height, terrace size, and surface roughness (σ_{rms}) using the Nanoscope software. σ_{rms} values typically have an uncertainty of $\pm$ 1 Å. Roughness values obtained from TMAFM images and from X-ray reflectivity have been shown to compare reasonably well (Munkholm et al., 1997; Fenter et al., 2000b).

3.3. X-ray Reflectivity

Quartz slabs were cleaned ultrasonically for 15 min in methanol and 15 min in deionized water, and rinsed thoroughly with deionized water. The slabs were then mounted in an X-ray reflectivity cell that uses an 8 μm-thick Kapton® (polyimide) membrane to maintain a thin film of water over the sample (Fig. 2; Fenter et al., 2000a, 2000b). Care was taken to ensure that the surface remained wet during the mounting

procedure. Preliminary reflectivity data were collected at bending magnet beamline 12-BM; however, the data shown below were all measured at undulator beamline 12-ID (BESSRC-CAT, Advanced Photon Source, Argonne National Laboratory). The undulator beamline was needed to obtain sufficient incident flux to measure the small reflectivities ($<10^{-10}$) of these surfaces in the presence of a finite background signal due to scattering from the plastic film and water layer. An X-ray energy of 19.50 keV (wavelength $\lambda = 0.6358$ Å) was selected by double reflection on a Si(111) monochromator. The incident beam size was reduced to 0.1 mm (vertically) by 0.2 mm (horizontally) with a pair of slits, and the detector aperture was 0.3 mm (vertically) by 3 mm (horizontally), resulting in an angular resolution for the detector of $\Delta 2\theta = 0.03°$ within the vertical scattering plane. The X-ray flux reflected by the quartz surfaces was measured at discrete values of Q by rocking-curve scans through the specular reflection condition. For these scans,
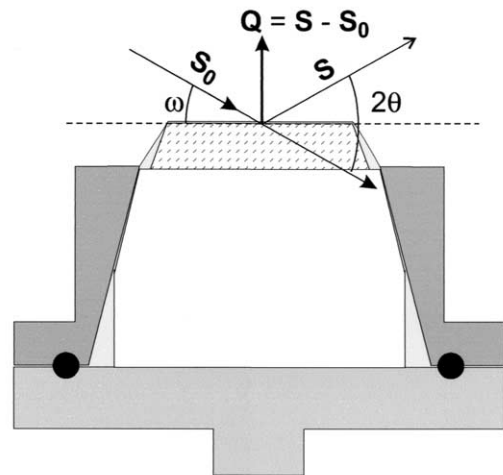

Fig. 2. Schematic representation of the thin film reflectivity cell and illustration of the experimental reflectivity geometry. The incident and the reflected X-ray beams, S_0 and S, respectively, are located in a plane perpendicular to the sample surface. Q is the momentum transfer. The specular reflection condition is $\omega = (2\theta)/2$.

Table 1. Structural data for quartz in the P3$_2$21 space group setting (from Kihara, 1990).

Unit cell		Atom positions[a]			
a (Å)	4.9137	x(O)	0.5867	x(Si)	0.5303
c (Å)	5.4047	y(O)	0.7328	y(Si)	0.000
		z(O)	0.7855	z(Si)	2/3

[a] Atom coordinates transformed from their original reverse setting to an obverse setting.

the detector is fixed in 2θ position (i.e., fixed Q value), and the angle ω between the incident beam and the crystal is scanned to obtain the integrated surface reflectivity. Reflectivities were determined by numerical integration of the peak areas after subtraction of a linearly-varying background signal. The reflectivity at reference points was measured periodically to insure that the interface remained stable during data acquisition. The surface was also checked by eye periodically to assess any visible modification. After several hours of exposure, darkening that penetrated ~ 1 mm into the crystal was observed within the beam footprint for all probed (10$\bar{1}$1) surfaces. The presence of this darkening within the quartz crystal indicates that it resulted from bulk solid modifications that may or may not have originated from an interfacial reaction. However, no changes in the reflected intensity were observed, suggesting that structural changes at the mineral-water interface were negligible. No darkening was observed for (10$\bar{1}$0) quartz surfaces, even after several hours of exposure. This observation suggests that (10$\bar{1}$1) planes may concentrate defects such as chemical impurities that interact with the X-rays to produce color centers (Rossman, 1994). Reflectivity data were recorded on two crystals for both natural (10$\bar{1}$0) and (10$\bar{1}$1) surfaces, and on only one crystal for the annealed (10$\bar{1}$0) and (10$\bar{1}$1) surfaces.

Reflectivity data were modeled using atomic structural models featuring quartz terminations obtained by breaking structural bonds along a plane parallel to the mineral-water interface, and then filling Si dangling bonds with oxygens. Atomic positions (Table 1) and Debye-Waller parameters for quartz were taken from Kihara (1990). Models were further refined by assuming a fixed bulk quartz structure at depths from the surface ≥ 15 Å, allowing positions of near-surface atoms to relax perpendicular to the surface, and by considering surface roughness as given by Eqn. (3 to 4), structured layers of water above the interface, and featureless bulk water above the structured layers (Fenter et al., 2000a, 2000b). Several relaxation models with distinct parametrizations were tested for the (10$\bar{1}$0) surfaces to test for uniqueness. These tests showed that features such as maximum depth of relaxation, the coordination and relaxation of surface atoms, and interfacial water properties were generally similar. The models presented in this paper were selected based on their conceptual simplicity and fit quality. The structural resolution of such models is a function of the range of measured momentum transfer and is approximated by $2\pi/Q_{max}$, where Q_{max} is the highest Q value at which reflectivity data are collected (Fenter et al., 2001). The quality of the data fit was assessed by the reduced chi factor $\chi^2 = (1/n)[\Sigma_Q(R(Q)_{exp} - R(Q)_{calc})/\sigma(Q)_{exp}]^2$, where n is the number of independent data points, and $R(Q)_{exp}$, $R(Q)_{calc}$ are respectively the experimental and calculated reflectivities, and $\sigma(Q)_{exp}$ is the experimental uncertainty on $R(Q)_{exp}$ resulting from X-ray counting statistics. The χ^2 value gives a quantitative measure of the total error per data point for a given model, and consequently $\chi^2 \sim 1$ when a model reproduces the data within the statistical error (that is, when the difference between $R(Q)_{exp}$ and $R(Q)_{calc}$ equals $\sigma(Q)_{exp}$ on average). The least-squares fitting procedure also provides a well-defined estimate for the uncertainty associated with each structural parameter in the model. Uncertainties are reported here at the 95% confidence level. The total number of fitted parameters (including those for water structure and surface roughness) is limited by the number of independent data points. It is common in bulk crystallographic measurements to have sufficient data to over-determine the structural determination with ~10 data points per fitted parameter to ensure a unique structural determination (Giacovazzo, 1992). This is often difficult to achieve in surface crystallography measurements, but as a rule of thumb, a ratio of about three to five data points per fitted parameter is considered

sufficient to determine a structure uniquely. The relaxation parameters obtained by this fitting procedure describe the vertical distribution of atom layers that are aligned parallel to the interface. Other techniques, such as non-specular X-ray reflectivity, are required to determine the lateral position of atoms, and provide a three-dimensional picture of the interface structure.

As we will describe below, the probed quartz surfaces have typical values of $\sigma_{rms} \sim 3$ Å. Such roughness would produce a ~ fivefold decrease in the reflectivity between bulk Bragg peaks compared to an ideal surface with $\sigma_{rms} = 0$ Å. Within this roughness regime, modification of the reflectivity due to steps, B(Q), becomes sensitive to the height distribution of terraces on the surface. This is a potential source of systematic error if the wrong form for B(Q) is assumed. The impact of the roughness model on the values of best-fit parameters was assessed by considering an alternate model of surface roughness in addition to that of Eqn. 4, assuming a discrete gaussian distribution of terrace heights separated by unit-cell high steps according to

$$P(nd_{(10\bar{1}1)}) = \exp(-[(nd_{10\bar{1}1} - z_{ref})/s]^2) \Big/ \sum_i \exp(-[(n_i d_{10\bar{1}1} - z_{ref})/s]^2),$$

(5)

where $P(nd_{(10\bar{1}1)})$ is the proportion of terrace surface exposed at an altitude $(nd_{(10\bar{1}1)})$, and z_{ref} and s are the distribution center and width, respectively. This alternate model resulted in best-fit results which were comparable (within uncertainty) to those obtained previously with Eqn. 4 with an overall deterioration in the quality of fit. Therefore, our reported structural parameters do not depend on the choice of roughness model. Reflectivity-derived roughness values given below were obtained using Eqn. 4.

4. RESULTS

4.1. Atomic Force Microscopy

AFM images of the natural (10$\bar{1}$1) surfaces (Fig. 3a,b) display flat terraces with typical widths ranging between ~ 0.1 and ~ 1 μm. These terraces are delimited by sinuous, and sometimes coalescing, steps following the [$\bar{2}\bar{3}2$] general direction given by the intersection of two symmetry-equivalent {10$\bar{1}$1} planes (Fig. 3a,b; white arrows). The measured heights of the smallest steps equal 3.4 ± 0.4 Å, in excellent agreement with the unit cell spacing normal to the (10$\bar{1}$1) plane ($d_{10\bar{1}1} = 3.341$ Å). The absence of steps of smaller height (e.g., $d_{10\bar{1}0}/2$) suggests that only one type of surface termination is exposed per image (Gratz and Bird, 1993a). Some 4×4 μm imaged areas display only unit-cell high steps (Fig. 3a), yet larger steps of 13 to 25 Å in height (~ 4 to 7 unit cells) running parallel to the [$\bar{2}\bar{3}$ 2] direction can also be observed on other images (Fig. 3b, black arrow), and may be interpreted as nm-sized {10$\bar{1}$1} microfacets. σ_{rms} values obtained from analysis of several areas with sizes from 1×1 to 4×4 μm typically ranged between 5 and 11 Å. This range compares well with the roughness value (~ 12 Å) derived from a 4×4 μm AFM image of the (001) cleavage surface of a gem-quality orthoclase from Itrongay, Madagascar (Fenter et al., 2000b). In an effort to evaluate the contribution to σ_{rms} of the small "bumps" that can be seen on the images (presumably originating from surface particles that survived the cleaning procedure), roughness was remeasured after masking these "bumps" from the analysis. This procedure resulted in a diminution of measured σ_{rms} to 66% of the initial values, suggesting that remaining "dust" particles can significantly contribute to the surface roughness measured by AFM. The residual roughness results only from the presence of steps, and is qualitatively different from the atomic roughness of
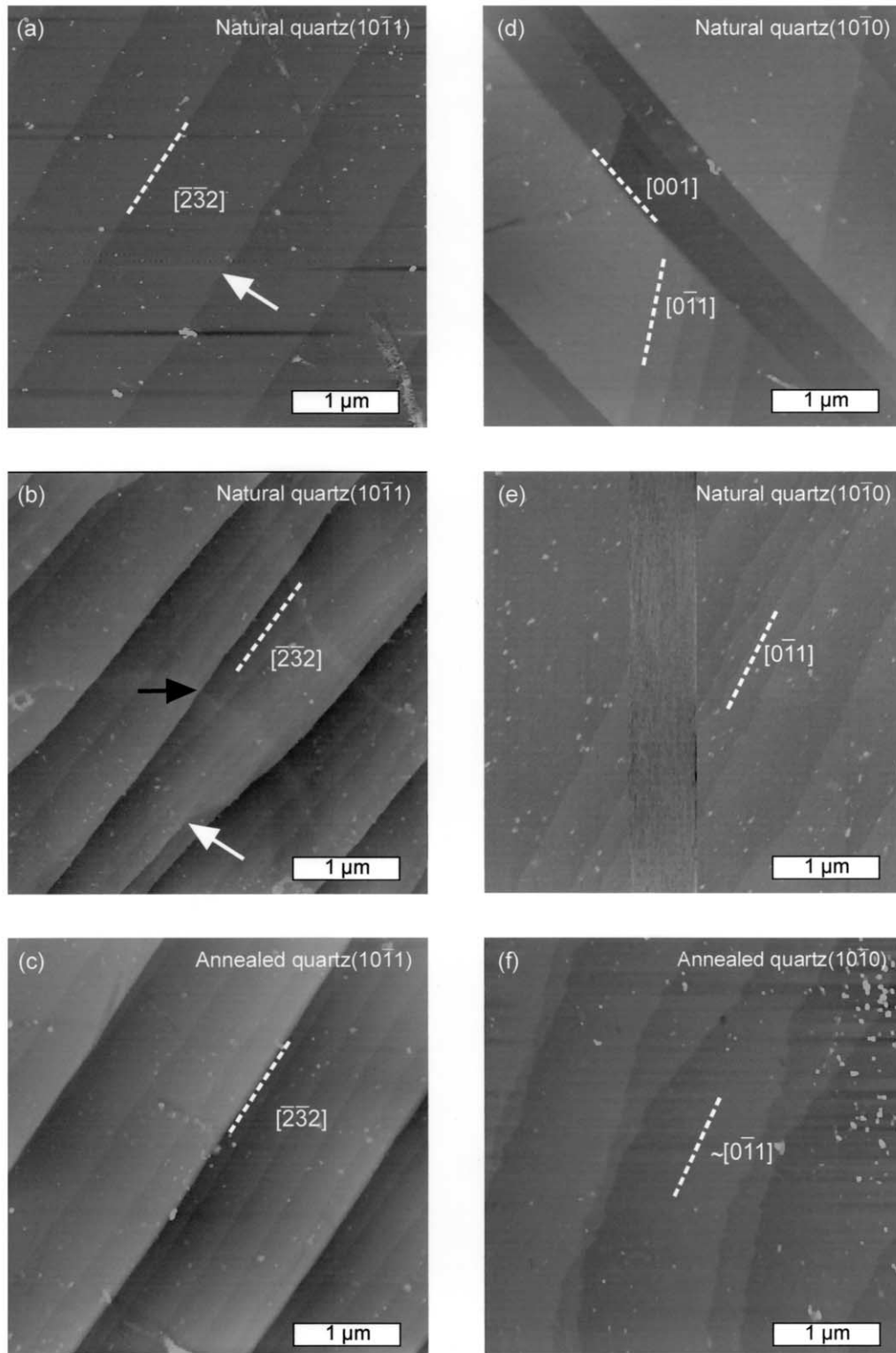
Fig. 3. TMAFM images of regions (4 μm by 4 μm) of quartz (10$\bar{1}$1) and (10$\bar{1}$0) surfaces. (a, b) Natural (10$\bar{1}$1) surface. (c) Annealed (10$\bar{1}$1) surface. (d, e) Natural (10$\bar{1}$0) surfaces. (f) Annealed (10$\bar{1}$0) surface. Image 3e was rotated by 90° to visually align in the figure all equivalent steps observed on (10$\bar{1}$0) surfaces. The vertical band near the central part of the image resulted from a temporary loss of contact between the AFM tip and the sample.

fused silica surfaces that is caused by the dispersion in height of structurally similar silica groups (Simpson et al., 1999).

Flat terraces with widths of 0.1 to 1 μm and separated by unit-cell high and higher steps can also be observed on annealed (10$\bar{1}$1) surfaces (Fig. 3c); however, no extended ($>4\times4$ μm) areas with only unit-cell high steps were observed. Because AFM images sample only a small fraction (few μm^2) of the surface area, it is not possible to say that such extended areas were absent. σ_{rms} values (uncorrected for dust) for the annealed sample ranged from 10 to 18 Å.

Natural and annealed (10$\bar{1}$0) surfaces of quartz display steps delimiting flat terraces of typical width ranging between 0.2 and as much as 4.3 μm (Fig. 3d–f). Step heights are integer multiples of $\sim$ 4.4 $\pm$ 0.4 Å, which, compared to the cell spacing normal to the (10$\bar{1}$0) plane (d$_{10\bar{1}0}$ = 4.2515 Å), is evidence for the presence of only one type of surface termination on the imaged samples. Several straight steps are visible on the natural surface (Fig. 3d), and were also observed on the annealed surface (not shown). They follow [001] and [0$\bar{1}$1] directions, corresponding to the intersections between (10$\bar{1}$0) and (01$\bar{1}$0) planes, and between (10$\bar{1}$0) and (01$\bar{1}$1) planes, respectively. Sinuous steps approximately parallel to [0$\bar{1}$1] can also be observed on natural surfaces (Fig. 3e), and are still present after annealing (Fig. 3f). Natural and annealed (10$\bar{1}$0) surfaces have comparable surface roughness (3 $\leq \sigma_{rms} \leq$ 7 Å and 3 $\leq \sigma_{rms} \leq$ 6 Å, respectively; uncorrected for dust). In summary, AFM images indicate that both natural and annealed (10$\bar{1}$1) and (10$\bar{1}$0) surfaces of quartz display structural features (unit-cell high steps and broad terraces) suggesting the persistence of quartz structural organization at the surface terminations. Identity of the quartz surface structure and quantitative data on the surface relaxation are obtained below by X-ray reflectivity.

4.2. X-ray Reflectivity Data

Typical rocking-curve scans obtained at selected Q values on the annealed (10$\bar{1}$0) face (Fig. 4) display narrow peaks over a linear background. Peak widths were determined by fitting a Gaussian peak shape and a linear background to the rocking-curve data. All peaks have a similar resolution-limited width at all Q values of $\Delta\omega$ = 0.015°, although the reflected amplitude spans several orders of magnitude. The presence of this significant X-ray reflectivity over a broad range of Q values, coupled with the absence of diffuse scattering near the specular direction (e.g., broadening of the rocking-curve peak, or presence of "tails") confirms that the quartz-water interfaces in the present study are molecularly flat. Comparable observations were made for the (10$\bar{1}$1) surface, indicating that (10$\bar{1}$1) quartz-water interfaces are also molecularly flat. Because the rocking curve shapes are not well-described by a Gaussian shape over the range of angles studied (e.g., see the rocking curve at Q = 1.58 Å^{-1} in Fig. 4), we used a numerical integration procedure to obtain the integrated intensities for each rocking curve, as described above.

Reflectivity data for annealed and natural (10$\bar{1}$1) and (10$\bar{0}$1) surfaces of quartz follow the trend expected for crystal truncation rods (CTRs; Robinson, 1986), with large reflectivity close to the Bragg peaks, and small, at times $<$ 10^{-10}, reflectivity between the Bragg peaks (Fig. 5). The reflectivity at the Bragg
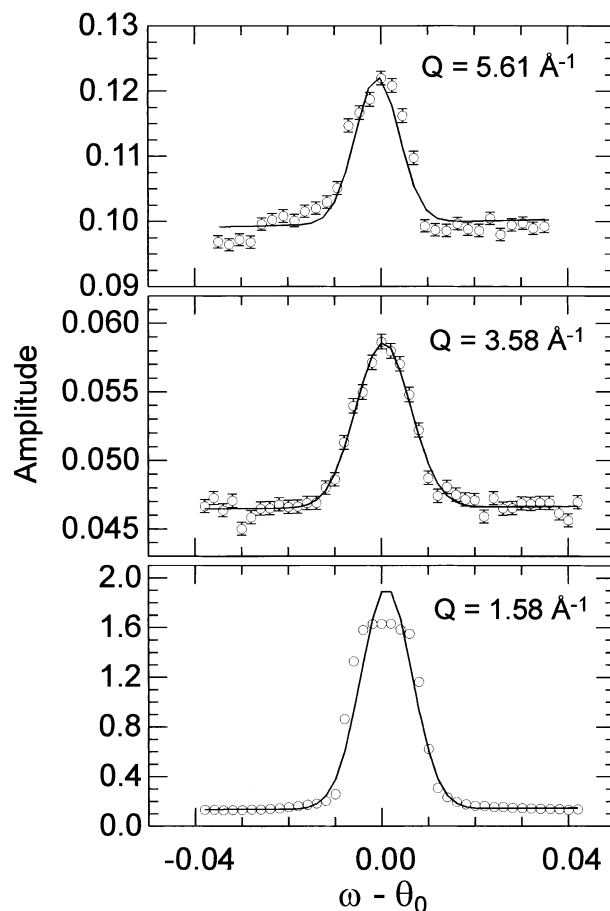

Fig. 4. Individual rocking curves and Gaussian fits for selected values of Q for the annealed (10$\bar{1}$0) surface. All peaks display similar resolution-limited widths within the statistical uncertainty of the data, although the reflectivity spans several orders of magnitude.

peak positions Q$_{10\bar{1}1}$ = 1.88 Å^{-1} and Q$_{10\bar{1}0}$ = 1.46 Å^{-1}, corresponds to Bragg plane spacings of d$_{10\bar{1}1}$ = 3.3418 Å and d$_{10\bar{1}0}$ = 4.2515 Å, respectively. Reflectivity data for annealed and natural (10$\bar{1}$1) surfaces have similar shapes, with reflectivity minima located at Q = 1.0 and 2.9 Å^{-1}. However, modest but significant differences between CTRs are observed in the relative variations in amplitude away from the Bragg peaks. For example, the reflectivity for the annealed (10$\bar{1}$1) surface [(10$\bar{1}$1)$_{ann}$] at Q $\sim$ 1 and 2.9 Å^{-1} is lower than that for both natural surfaces [(10$\bar{1}$1)$_{nat1}$ and (10$\bar{1}$1)$_{nat2}$; Fig. 5a]. The relative symmetric decrease of the midzone intensity (e.g., near $\sim$1 and 3 Å^{-1}) suggests that this amplitude difference results from greater surface roughness for (10$\bar{1}$1)$_{ann}$. While the CTRs for annealed [(10$\bar{1}$0)$_{ann}$] and natural [(10$\bar{1}$0)$_{nat2}$] (10$\bar{1}$0) surfaces retain approximately the same shapes, slight amplitude differences can also be noted between these data, e.g., at Q = 1.0, and 3.75 Å^{-1} (Fig. 5b). In contrast, the CTR for (10$\bar{1}$0)$_{nat1}$ is distinctive and shows substantial amplitude decreases near Q = 0.8, 2.0 and 3.5 Å^{-1}. In summary, except for (10$\bar{1}$0)$_{nat1}$, CTRs for annealed and natural surfaces of the same orientations have mostly comparable shapes, albeit with some minor variations in amplitude. How these observations are related to the surface
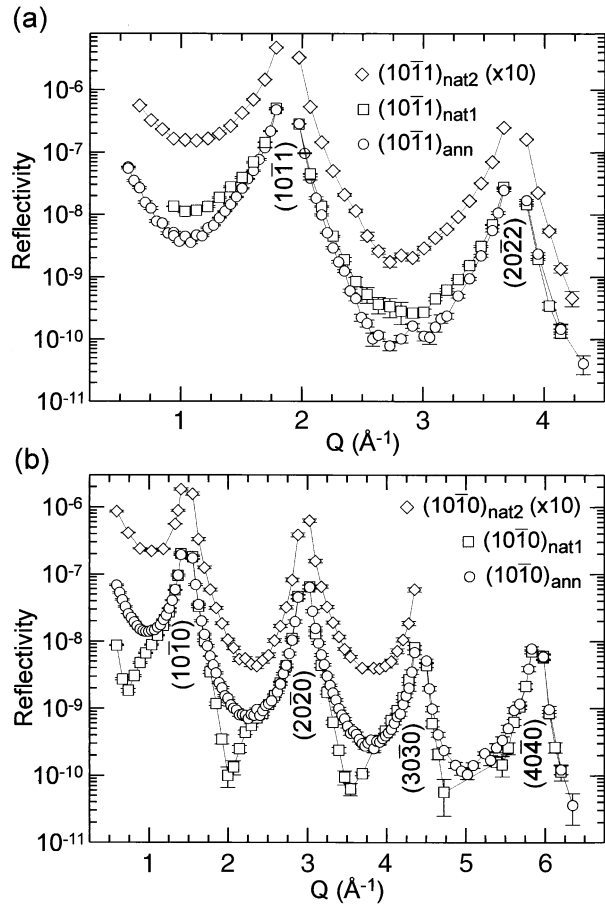
Fig. 5. Comparison of reflectivity data between annealed and natural surfaces of quartz. Lines are guides to the eye. (a) Natural [(10$\bar{1}$1)$_{nat1}$: □, and (10$\bar{1}$1)$_{nat2}$: ◇] and annealed [(10$\bar{1}$1)$_{ann}$: ○] (10$\bar{1}$1) surfaces. (b) Natural [(10$\bar{1}$1)$_{nat1}$: □, and (10$\bar{1}$0)$_{nat2}$: ◇] and annealed [(10$\bar{1}$0)$_{ann}$: ○] (10$\bar{1}$0) surfaces. Note that data for (10$\bar{1}$0)$_{nat1}$ systematically display reflectivity minima on the high Q side of Bragg peaks. Amplitudes for (10$\bar{1}$1)$_{nat2}$ and (10$\bar{1}$0)$_{nat2}$ have been multiplied by 10.

terminations and structural properties of the mineral-water interfaces is examined next.

4.2.1. Reflectivity of the (10$\bar{1}$1) quartz-water interface

A model surface termination for the (10$\bar{1}$1) face was obtained by breaking bonds parallel to the (10$\bar{1}$1) plane (Fig. 6a) and then filling Si dangling bonds with oxygens. Using the notation of Figure 6a, the surface termination that yielded the preliminary best fit to the reflectivity data was obtained by breaking the bonds between O$_5$ and Si$_1$, and between O$_6$ and Si$_2$. Note that this termination coincides with the minimum number of truncated bonds per unit cell, as other surface terminations would cleave at least three Si-O bonds. Also, each surface silicon atom binds to three oxygens from other silicon tetrahedra (3c groups), as surmised by Gratz and Bird (1993a). Further modeling of the reflectivity data was performed by relaxing the position of Si and O atoms located near the interface. As Q$_{max}$ = 4.2 Å^{-1} for (10$\bar{1}$1) surfaces, the resolu-
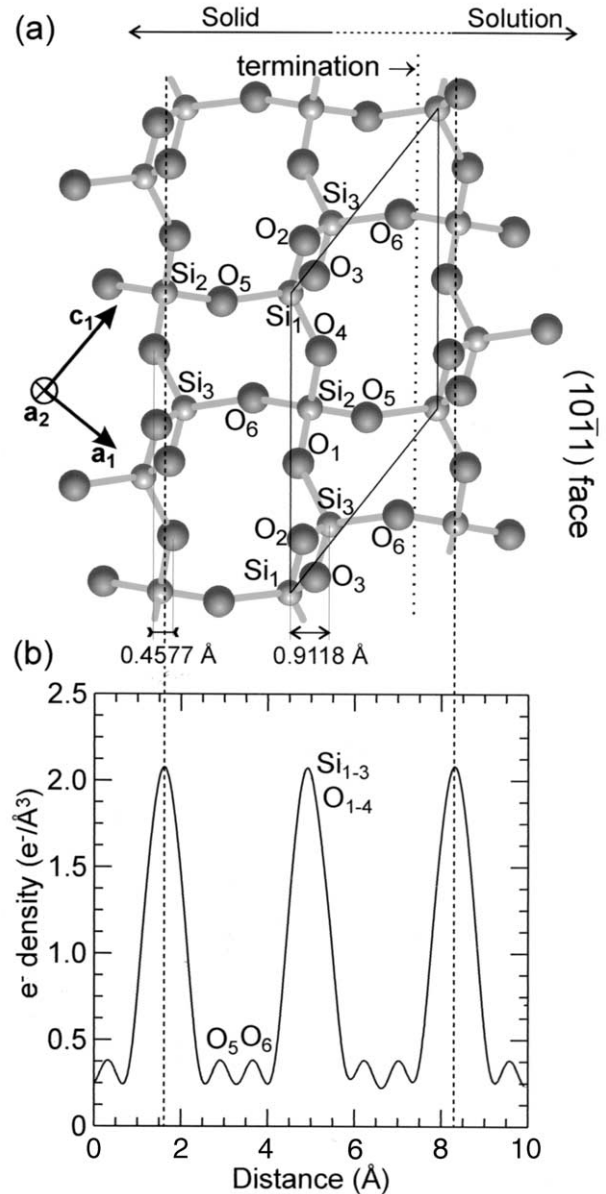

Fig. 6. (a) Atomic structure of quartz projected along the **a$_2$** direction, and (10$\bar{1}$1) termination plane minimizing the number of truncated oxygens. (b) Laterally-averaged electron density profile parallel to the (10$\bar{1}$1) plane at a resolution of $2\pi/4.2 \approx 1.5$ Å.

tion of the reflectivity data equals 1.5 Å, which causes the electronic contributions from individual atomic layers to overlap, as is the case e.g., for Si$_{1-3}$ and O$_{1-4}$ (Fig. 6b). Therefore, individual relaxation parameters for these atoms should be considered cautiously. In contrast, electron density maxima from O$_5$ and O$_6$ are well resolved, and relaxation parameters for these are more reliable. Additionally, the number of independent data points limits the number of fitting parameters that can be reasonably applied to fitting the data. To account for these limitations, only the relaxation parameters for Si were allowed to vary independently, while those for oxygens ligated to two Si atoms were constrained to

$$\delta O_1(i) = [\delta Si_2(i) + \delta Si_3(i)]/2; \qquad (6a)$$

$$\delta O_2(i) = [\delta Si_1(i) + \delta Si_3(i)]/2; \qquad (6b)$$

$$\delta O_3(i) = [\delta Si_1(i) + \delta Si_3(i)]/2; \qquad (6c)$$

$$\delta O_4(i) = [\delta Si_1(i) + \delta Si_2(i)]/2; \qquad (6d)$$

$$\delta O_5(i) = [\delta Si_2(i) + \delta Si_1(i-1)]/2; \qquad (6e)$$

$$\delta O_6(i) = [\delta Si_3(i) + \delta Si_2(i-1)]/2; \qquad (6f)$$

where, for example, $\delta O_1(i)$ is the vertical displacement of the O_1 atom in the ith unit cell layer, and i = 1 for the outermost unit cell layer. $O_5(1)$ and $O_6(1)$ at the quartz surface are bonded to only one Si each ($Si_2(1)$ and $Si_3(1)$, respectively), and they are presumably hydroxylated; therefore, their relaxations were fitted independently. In the following presentation, the annealed surface is considered first.

The above parameterization allowed a good model fit of the $(10\bar{1}1)_{ann}$ CTR (Fig. 7a,b), with $\chi^2 = 2.50$. Relaxation occurred to a depth of four unit cells (13.4 Å), and involved 10 structural parameters, yielding a ratio of number of independent data points to parameters (including those for adsorbed and bulk water structure and surface roughness) equal to $61/20 \approx 3.05$. This ratio is at the low end of values for which relaxation profiles near the surface can be uniquely determined from the data set. Allowing structural relaxation below 13.4 Å resulted in insignificant relaxation values, thereby unnecessarily increasing the number of fitted parameters.

The best fit included the contribution of $O_5(1)$ and $O_6(1)$ oxygens, resulting in a well-resolved peak in the electron density profile (Fig. 7c). Attempts to remove either of these surface oxygens resulted in a poorer quality of fit. This confirms the presence of surface oxygens, which presumably are hydroxylated. Another significant feature of the best-fit model for the $(10\bar{1}1)_{ann}$ surface is the small ($\leq \pm$ 0.1 Å) relaxation occurring in the solid, except for the most external Si and the surface oxygens, which relax toward the solution and the surface, respectively (Fig. 7d). Within uncertainties, the distances measured between $Si_2(1)$ and $O_5(1)$ planes (1.1 ± 0.2 Å), and between $Si_3(1)$ and $O_6(1)$ planes (1.2 ± 0.3 Å) are equal to or slightly lower than the same distances measured for equivalent atomic positions in the bulk structure (1.2950 and 1.5968 Å, respectively; Table 2). Decreased distances might result from several distortion mechanisms such as tilting of the Si-O bonds toward the surface, or formation of hydrogen bridges between silanol H and water oxygen, resulting in weaker O-H interactions and stronger Si-O interactions, ultimately shortening Si-O distances.

An adsorbed layer of water is consistent with measured electron density profiles and consists of 1.8 ± 0.15 molecules/33.80 Å^2 at 2.8 ± 0.2 Å beyond $Si_3(1)$, that is, 1.6 ± 0.2 Å beyond the surface hydroxyl groups. This distance is greater than the Debye-Waller parameter for water u_{W1} = 0.72 Å, a measure of the root mean-square height distribution of water, implying that most adsorbed water remains mainly as a separate layer above the surface oxygens. This is consistent with the presence of some free volume at the quartz surface. Two silanol groups with an effective two-dimensional cross-section of ~ 10.6 Å^2 each are present/33.80 Å^2, leaving ~ 35% of the
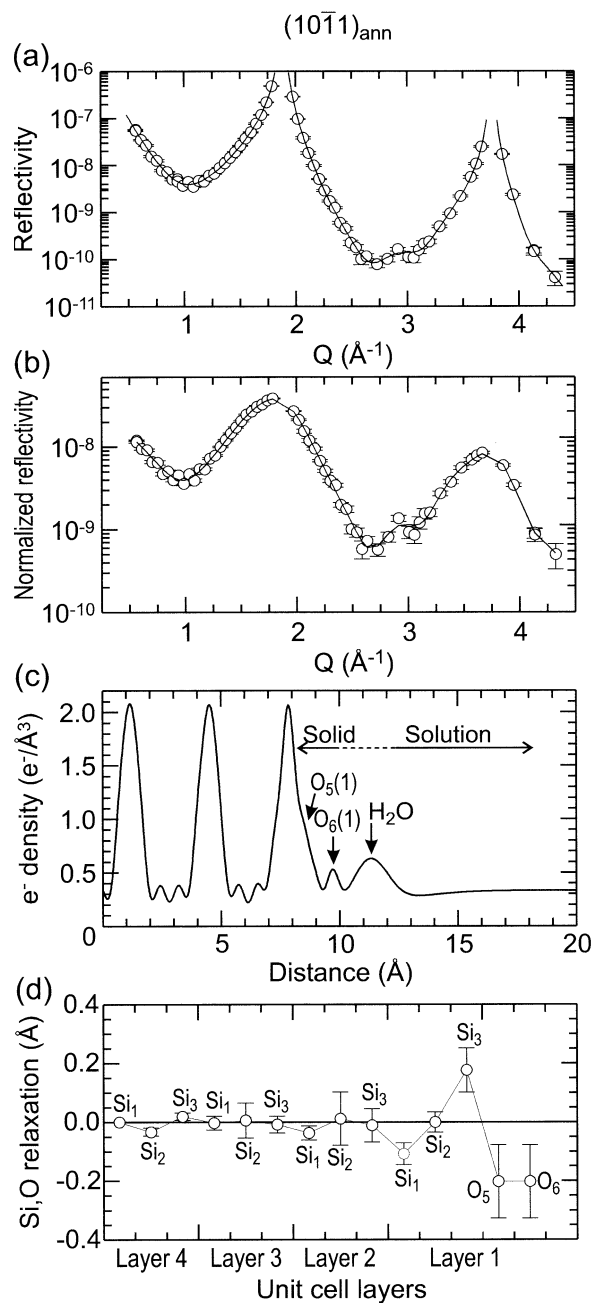

Fig. 7. Best fit results for X-ray reflectivity data obtained at the annealed $(10\bar{1}1)$ surface. (a) Reflectivity data R(Q) and best fit. (b) Normalized data $R(Q)\cdot[Qsin(Qd_{10\bar{1}1}/2)]^2$ and best fit. Normalization highlights the contribution of the interfacial structure (and not surface roughness) to the reflectivity data. (c) Laterally-averaged electron density profile; $O_5(1)$ and $O_6(1)$ indicate the O_5 and O_6 atoms in the surface layer, respectively. (d) Relaxation parameters as a function of the unit cell layer. Positive and negative relaxations are toward the solution and the bulk crystal, respectively.

silica network directly exposed to the solution. No oscillations in the electron density profile of water could be observed beyond this adsorbed layer, ruling out structural layering of water in the solution at the resolution of the data. Finally, the surface roughness, as calculated from the β parameter, equals

Table 2. Reflectivity-derived structural parameters for the quartz $(10\bar{1}1)$ water interface. All distances are measured perpendicular to the reflection plane.

Sample	Roughness (Å)	$d_\perp Si_2$-O_5[a] (Å)	$d_\perp Si_3$-O_6[b] (Å)	$d_\perp Si_3$-W1[c] (Å)	$d_\perp O_6$-W1 (Å)	$d_\perp O_6$-W2[d] (Å)	N_{w1}[e] (33.80 Å^{-1})	u_{w1} (Å)	χ^2
$(10\bar{1}1)_{ann}$	3.0 ± 0.2	1.1 ± 0.2	1.2 ± 0.3	2.8 ± 0.2	1.6 ± 0.2	3.2 ± 0.5	1.8 ± 0.15	0.72[f]	2.50
$(10\bar{1}1)_{nat1}$	1.8 ± 0.5	1.05 ± 0.7	1.27 ± 0.7	2.9 ± 0.5	1.6 ± 1.1	3.2 ± 1.8	2.3 ± 0.5	0.72[f]	1.36
$(10\bar{1}1)_{nat2}$	1.8 ± 0.6	1.0 ± 0.4	1.1 ± 0.4	2.5 ± 0.3	1.7 ± 0.6	2.3 ± 1.2	2.0 ± 0.4	0.72[f]	2.48

[a] Bulk structural value 1.2950 Å.
[b] Bulk structural value 1.5968 Å.
[c] Distance between the $Si_3(1)$ layer and the first layer of adsorbed water (W1).
[d] Distance between the $O_6(1)$ layer and W2, the water layer directly above W1.
[e] Surface occupancy of water in the W1 layer.
[f] u_w values are sometimes poorly constrained. Here, they were fixed during the fitting procedure.

3.0 ± 0.2 Å, which is slightly lower than σ_{rms} values from AFM ($5 \leq \sigma_{rms} \leq 11$ Å). Keeping in mind that our AFM measurements overestimate the surface roughness because of the presence of "dust," the fair agreement between surface roughness measured by AFM and reflectivity suggests that most of the structural roughness on annealed $(10\bar{1}1)$ is present at a scale accessible to AFM, e.g., in the form of unit-cell high steps.

The similarities between the CTRs for annealed and natural $(10\bar{1}1)$ surfaces of quartz suggested that comparable relaxation models should apply to both surfaces. Indeed, good fits were obtained for $(10\bar{1}1)_{nat1}$ (kept in water for 10 months before reflectivity measurements) and $(10\bar{1}1)_{nat2}$ ($\chi^2 = 1.36$ and 2.48, respectively; Fig. 8a,b) with insignificantly different electron density profiles (Fig. 8c) and structural parameters for the mineral-water interface (Fig. 8d and Table 2) that compare fairly well with those obtained for $(10\bar{1}1)_{ann}$. The amount of water in the adsorbed layer also compares fairly well with that observed on $(10\bar{1}1)_{ann}$. This similarity allows us to place confidence in the model parameters, although the ratio of independent data points to model parameters ($33/19 \approx 1.74$ and $38/17 \approx 2.24$ for $(10\bar{1}1)_{nat1}$ and $(10\bar{1}1)_{nat2}$, respectively) is clearly lower than appropriate for unique determination of the relaxation profile. Note that the number of parameters was lower for the natural surface because the modeled relaxation of Si_1 in layer 4 was negligible: therefore, $Si_1(4)$ was fixed at its bulk crystallographic position. The difference in the number of data points resulted in part from the higher number of data points collected at low Q for $(10\bar{1}1)_{nat2}$ (Fig. 8a), and in part from the greater density of data points per Bragg zone for $(10\bar{1}1)_{ann}$ compared to the natural surfaces (Fig. 7a and 8a). The similar relaxation patterns observed for the natural and annealed surfaces indicate that the $(10\bar{1}1)$ surface has not undergone extensive structural modifications upon annealing. Roughness values for $(10\bar{1}1)_{nat1}$ (1.8 ± 0.5 Å) and $(10\bar{1}1)_{nat2}$ (1.8 ± 0.6 Å) are slightly lower than that for $(10\bar{1}1)_{ann}$ (3.0 ± 0.2 Å), and also lower than σ_{rms} values measured from AFM images for $(10\bar{1}1)_{ann}$ ($10 \leq \sigma_{rms} \leq 18$ Å). This implies that storage of the $(10\bar{1}1)_{nat2}$ sample in water for 10 months had no significant effect on the roughness, structure, or termination of the quartz surface. The differences in height and occupation of the adsorbed water layer for the two natural and one annealed surfaces are within the derived error of each other.

4.2.2. Reflectivity of the $(10\bar{1}0)$ quartz-water interface

Two distinct surface terminations may be obtained theoretically by breaking the same number of bonds at the $(10\bar{1}1)$ quartz surface, and then filling Si dangling bonds with oxygens (Fig. 9a). Termination α is obtained by truncating O_a-Si_b and O_b-Si_c bonds; Si_a atoms are therefore exposed at the surface and form only two crystal bonds with bulk silicon tetrahedra (2c groups). Termination β results from cleavage of O_e-Si_a and O_f-Si_a bonds; Si_b and Si_c are exposed at the surface and each forms 3c groups. To identify the $(10\bar{1}0)$ surface termination from our data, model reflectivities for unrelaxed, hydroxylated terminations α and β capped by a water layer were calculated, and compared to the $(10\bar{1}0)_{ann}$ CTR. The sensitivity to crystal termination is often found at small Q and especially near the first Bragg peak position (Fenter et al., 2000b). However, Figure 10 a shows that CTRs calculated for terminations α and β are similar for $Q < 3$ Å^{-1} and differ in intensity only at large Q, e.g., at 3.75 and 5 Å^{-1}. The similarity of these calculations for $Q < 3$ Å^{-1} in this case is the result of a particular symmetry of electron density normal to the surface in which the Si_a position is exactly halfway between the Si_{b-c} layers. Therefore, the calculated X-ray reflectivities of these two surface terminations are indistinguishable at small Q. However, there are differences in the calculated reflectivities at large Q if we assume that all silicon atoms are fully coordinated with oxygen atoms. The recalculated reflectivity for termination α clearly underestimates the data at high Q, as confirmed by $\chi^2 = 57.15$, whereas that calculated for termination β matches the overall CTR shape, an agreement supported by $\chi^2 = 6.19$.

To further refine the model for termination β, Si and O atoms were relaxed with respect to their bulk positions. Because of the high resolution, it is possible to determine the relaxation for individual oxygen layers. To reduce the number of fitting parameters, the positions of silicon atoms were correlated to those of relaxed oxygens. Relaxation parameters for Si are thus

$$\delta Si_a(i) = [\delta O_a(i) + \delta O_b(i) + \delta O_e(i + 1) + \delta O_f(i + 1)]/4,$$

(7a)

$$\delta Si_b(i) = [\delta O_a(i) + \delta O_c(i) + \delta O_d(i) + \delta O_e(i)]/4, \quad (7b)$$

$$\delta Si_c(i) = [\delta O_b(i) + \delta O_c(i) + \delta O_d(i) + \delta O_f(i)]/4, \quad (7c)$$

where for example, $\delta Si_a(i)$ is the vertical displacement of the Si_a atom in the ith unit cell layer and $i = 1$ for the most external
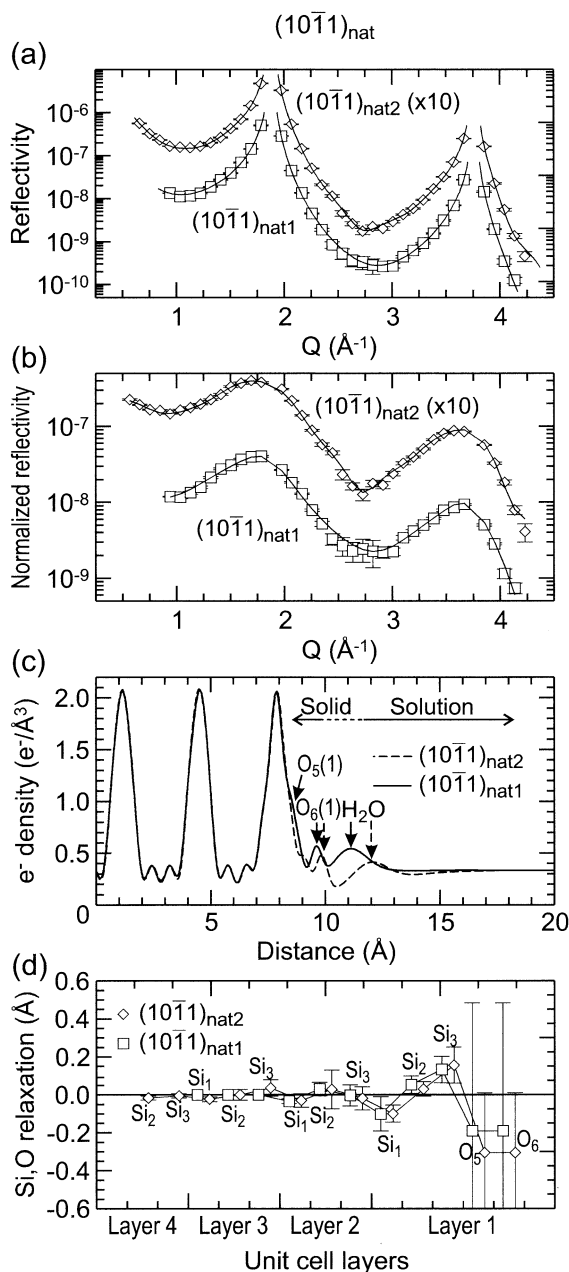
Fig. 8. Best fit results for X-ray reflectivity data obtained at natural $(10\bar{1}1)$ surfaces. (a) Reflectivity data R(Q) and best fit for $(10\bar{1}1)_{nat1}$ ($\square$) and $(10\bar{1}1)_{nat2}$ ($\diamond$; amplitudes multiplied by 10). (b) Normalized reflectivity data R(Q)·$[Qsin(Qd_{10\bar{1}1}/2)]^2$ and best fits for $(10\bar{1}1)_{nat1}$ ($\square$) and $(10\bar{1}1)_{nat2}$ ($\diamond$; amplitudes multiplied by 10). (c) Laterally-averaged electron density profiles; $O_5(1)$ and $O_6(1)$ indicate the O_5 and O_6 atoms in the surface layer, respectively. (d) Relaxation parameters for $(10\bar{1}1)_{nat1}$ ($\square$) and $(10\bar{1}1)_{nat2}$ ($\diamond$; offset toward right) as a function of the unit cell layer. Positive and negative relaxations are toward the solution and the bulk crystal, respectively.

unit cell. Relaxation for $(10\bar{1}0)_{nnn}$ occurred over two unit cell layers, or a total depth of 8.5 Å. A good fit ($\chi^2 = 1.32$; Fig. 10a,b) was obtained with a ratio of number of independent data points to fitting parameters equal to 120/21 = 5.7. Therefore, the best-fit results are expected to reflect the true structure of $(10\bar{1}0)_{ann}$.
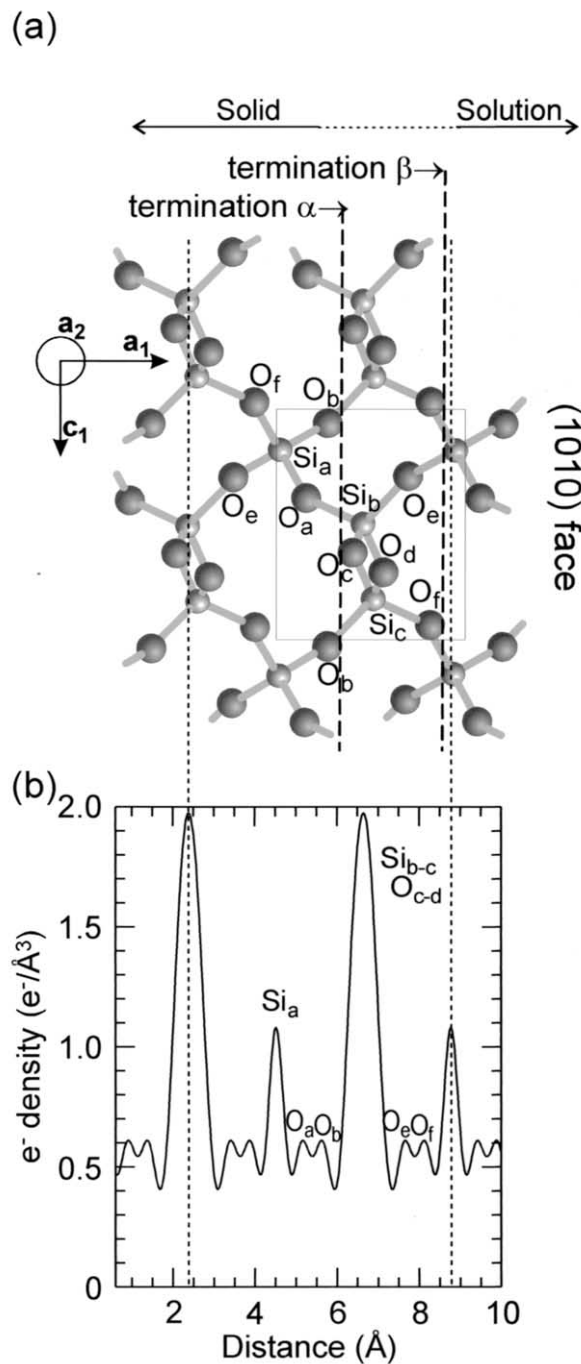

Fig. 9. (a) Atomic structure of quartz projected along the a_2 direction. Termination planes α and β minimizing the number of truncated oxygen bonds are also shown. (b) Laterally-averaged electron density profile at a resolution of $2\pi/6.2 \approx 1.0$ Å.

As for $(10\bar{1}1)$ quartz surfaces, oxygens from (presumably) silanol groups are present at the $(10\bar{1}0)$ quartz surface and account for a peak in the electron density profile (Fig. 10c). The distance between $Si_c(1)$ and $O_f(1)$ layers (1.36 ± 0.05 Å) compares with that observed in the solid (1.3758 Å), while that between $Si_b(1)$ and $O_e(1)$ layers (1.25 ± 0.04 Å) is slightly greater than that observed in the bulk structure (1.1186 Å;
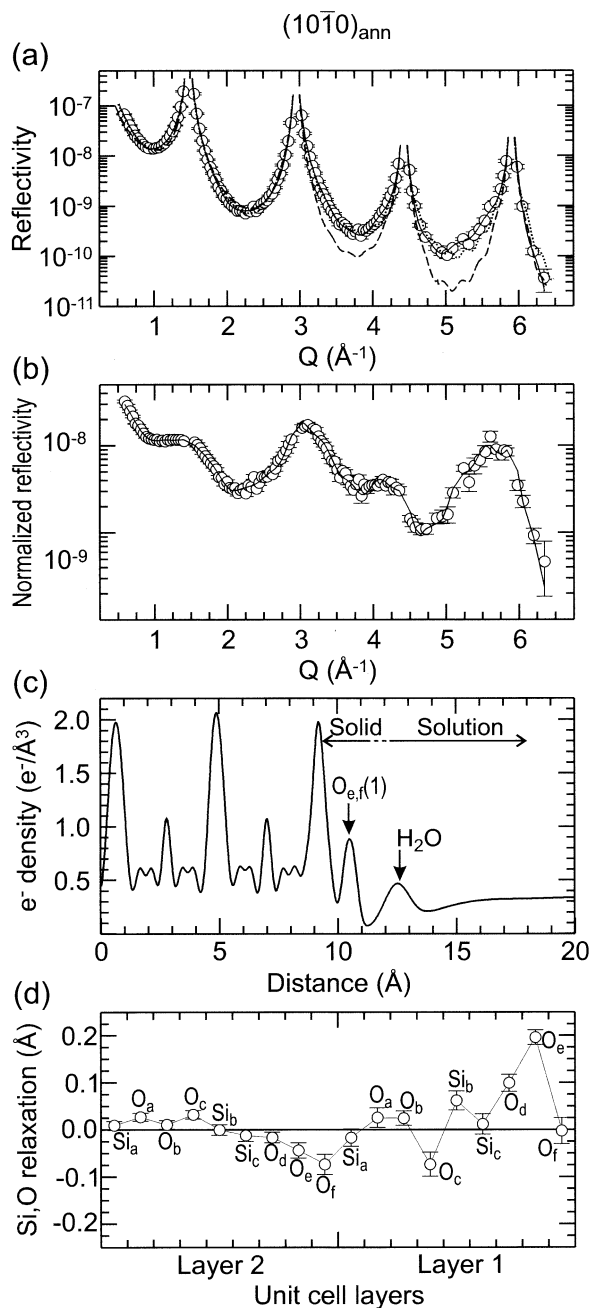
Fig. 10. Best fit results for X-ray reflectivity data obtained at the annealed $(10\bar{1}0)$ surface. (a) Reflectivity data R(Q) and best fit (solid line). Also shown are the CTRs for unrelaxed terminations α (dashed line) and β (dotted line). (b) Normalized reflectivity data $R(Q) \cdot [Q\sin(Qd_{10\bar{1}0}/2)]^2$ and best fit. (c) Laterally-averaged electron density profile; $O_{e,f}(1)$ indicates the $O_{e,f}$ atoms in the surface layer. (d) Relaxation parameters as a function of the unit cell layer. Positive and negative relaxations are toward the solution and the bulk crystal, respectively.

Table 3). This increase in distance might result from a distortion mechanism such as tilting of the Si-O bonds. Other significant features of the best-fit model include the small (<0.1 Å) relaxation in the solid, except for $O_d(1)$ and $O_e(1)$. The first layer of water contains 1.6 ± 0.15 molecules per $A_{10\bar{1}0}$ ($A_{10\bar{1}0}$

= 26.57 Å^2) at 3.2 ± 0.1 Å beyond $Si_c(1)$ that is, 1.83 ± 0.08 Å beyond the surface hydroxyl groups ($u_{W1} = 0.5 \pm 0.7$ Å). Both the surface coverage and the distance between the adsorbed water molecules and the external silanol groups agree with our model of the quartz $(10\bar{1}1)$ surface. Finally, the X-ray reflectivity surface roughness (3.3 ± 0.2 Å) compares remarkably well with σ_{rms} values obtained by AFM ($3 \leq \sigma_{rms} \leq 6$ Å), indicating a molecularly flat quartz surface.

The resemblance of the CTR shapes for $(10\bar{1}0)_{nat2}$ and $(10\bar{1}0)_{ann}$ suggests that the same relaxation model can be used for both surfaces. To further compare relaxation profiles, the parameterization used for $(10\bar{1}0)_{ann}$ relaxation was applied to $(10\bar{1}0)_{nat2}$, although the resolution is lower in the latter case. To decrease the degrees of freedom of the fit, relaxation was limited to the external unit cell layer. An excellent fit was obtained ($\chi^2 = 1.06$; Fig. 11a,b), but the ratio of independent data points to fitting parameters equals $44/16 = 2.75$, which is minimal and indicates that the best-fit model might not uniquely represent the data. Keeping this limitation in mind, electron density profiles for $(10\bar{1}0)_{ann}$ and $(10\bar{1}0)_{nat2}$ compare well (Fig. 10c and 11c), and similar atom relaxations are observed for the most external layers (Fig. 10d and 11d). Within uncertainty, the distance parameters for $O_e(1)$ and $O_f(1)$, as well as for adsorbed water, equal those obtained for $(10\bar{1}0)_{ann}$ (Table 3), again pointing to similar surface structures. However, the fitted number of adsorbed water molecules per $A_{10\bar{1}0}$ is slightly lower for the natural sample (1.2 ± 0.15; $u_{W1} = 0.5 \pm 0.2$ Å) than for the annealed one (1.6 ± 0.15). Finally, the reflectivity-derived surface roughness for this natural sample (2.7 ± 0.3 Å) is at the lower end of σ_{rms} values derived from the AFM analysis ($3 \leq \sigma_{rms} \leq 7$ Å). In conclusion, although some structural parameters for $(10\bar{1}0)_{ann}$ and $(10\bar{1}0)_{nat2}$ differ in detail, best-fit results for both surfaces are similar, indicating that annealing does not significantly affect the structure of this interface.

The CTR for $(10\bar{1}0)_{nat1}$ differs markedly from that of $(10\bar{1}0)_{ann}$ and $(10\bar{1}0)_{nat2}$ (Fig. 5b). Also, neither of the surface terminations α or β alone can fully account for the overall shape of the CTR, especially for the minima near $Q = 0.8$, 2.0, 3.5 and 4.7 Å^{-1}. Qualitatively, the strong decrease of the reflectivity indicates the presence of a layer that has approximately half the density of the layers in the substrate. Since these minima are systematically shifted to smaller Q with respect to the center of each midzone, this surface layer should have a height that is modestly larger than the substrate lattice spacing. With this in mind, the CTR shape may be explained by the coexistence of both terminations α and β at the $(10\bar{1}0)$ surface. With this assumption, a good fit ($\chi^2 = 1.54$) was obtained by assuming a coherent sum of 33 ±3% of termination α and 67 ±3% of termination β (Fig. 12a,b). Note, however, that the distance between $Si_b(1)$ and $O_e(1)$ layers (1.35 ± 0.08 Å) is larger than the equivalent distances measured in the bulk structure (1.1186 Å), while that measured between $Si_c(1)$ and $O_f(1)$ layers equals the bulk unrelaxed distance within uncertainty (1.47 ± 0.13 and 1.3758 Å, respectively; Table 3). Interestingly, the distances between $Si_a(1)$ and $O_a(1)$ and $O_b(1)$ layers (0.58 ± 0.4 and 1.20 ± 0.06 Å, respectively) match the distances measured between equivalent atoms in the bulk structure (0.6211 and 1.1360 Å, respectively). Also, the total adsorbed water, summed on terminations α and β, amounts to 2.8

Table 3. Reflectivity-derived structural parameters for the quartz (10$\bar{1}$0) water interface. All distances are measured perpendicular to the reflection plane..

Sample	Roughness (Å)	$d_\perp Si_b$-O_e[a] (Å)	$d_\perp Si_c$-O_r[b] (Å)	$d_\perp Si_c$-W1 (Å)	$d_\perp O_f$-W1[c] (Å)	$d_\perp O_f$-W2[d] (Å)	$d_\perp Si_a$-O_a[e] (Å)	$d_\perp Si_a$-O_b[f] (Å)	$d_\perp O_b$-W1[c] (Å)	$d_\perp O_b$-W2[g] (Å)	N_{w1}[h] (26.57 Å^{-1})	u_{w1} (Å)	χ^2
(10$\bar{1}$0)$_{ann}$	3.3 ± 0.2	1.25 ± 0.04	1.36 ± 0.05	3.2 ± 0.1	1.83 ± 0.08	5.0 ± 0.3					1.6 ± 0.15	0.5 ± 0.7	1.32
(10$\bar{1}$0)$_{nat1}$	3.6 ± 0.3	1.35 ± 0.08	1.47 ± 0.13	2.6 ± 0.2	1.2 ± 0.2	4.2 ± 0.4	0.58 ± 0.04	1.20 ± 0.06	2.4 ± 0.4	5.6 ± 0.4	2.8 ± 0.4	0.7 ± 0.1	1.54
(10$\bar{1}$0)$_{nat2}$	2.7 ± 0.3	1.20 ± 0.11	1.44 ± 0.17	3.4 ± 0.2	1.9 ± 0.2	4.7 ± 0.5					1.2 ± 0.15	0.5 ± 0.2	1.06

[a] Bulk structural value 1.1186 Å.
[b] Bulk structural value 1.3758 Å.
[c] Distance between the surface oxygens and the first layer of adsorbed water (W1).
[d] Distance between the $O_f(1)$ layer and W2, the layer of water directly above W1.
[e] Bulk structural value 0.6211 Å.
[f] Bulk structural value 1.1360 Å.
[g] Distance between the $O_b(1)$ layer and W2, the layer of water directly above W1.
[h] Surface occupancy of water in the W1 layer.

(a) $(10\bar{1}0)_{nat2}$

(a) $(10\bar{1}0)_{nat1}$
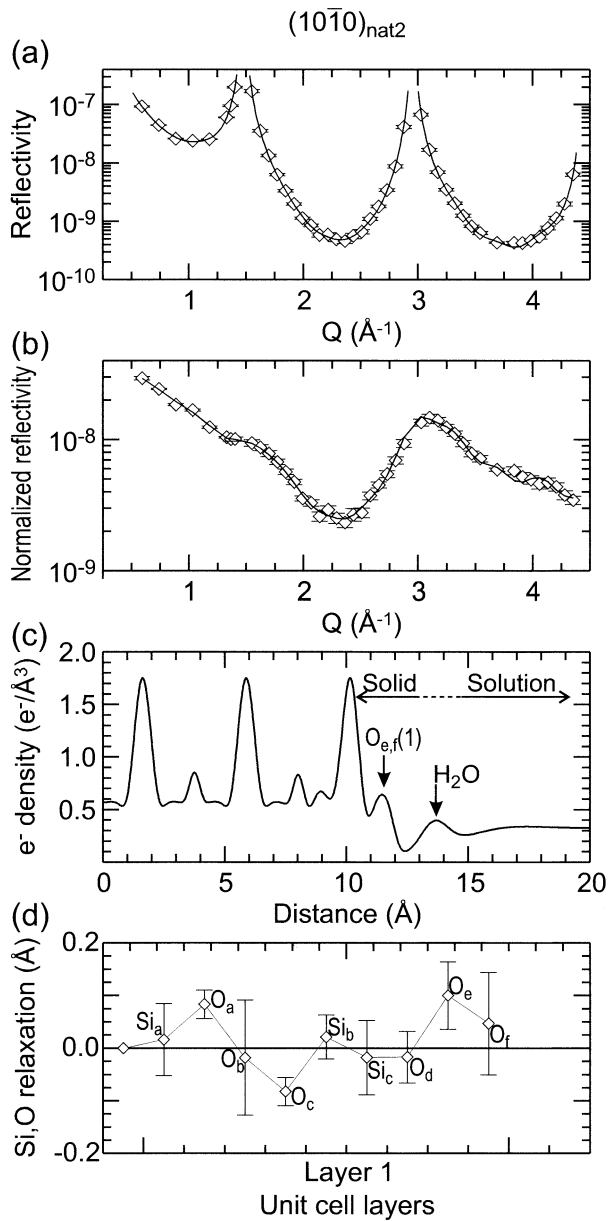

Fig. 11. Best fit results for X-ray reflectivity data obtained for the $(10\bar{1}0)_{nat2}$ natural surface. (a) Reflectivity data R(Q) and best fit. (b) Normalized reflectivity data $R(Q)\cdot[Qsin(Qd_{10\bar{1}0}/2)]^2$ and best fit. (c) Laterally-averaged electron density profile; $O_{e,f}(1)$ indicates the $O_{e,f}$ atom in the surface layer. (d) Relaxation parameters as a function of the unit cell layer. Positive and negative relaxations are toward the solution and the bulk crystal, respectively.
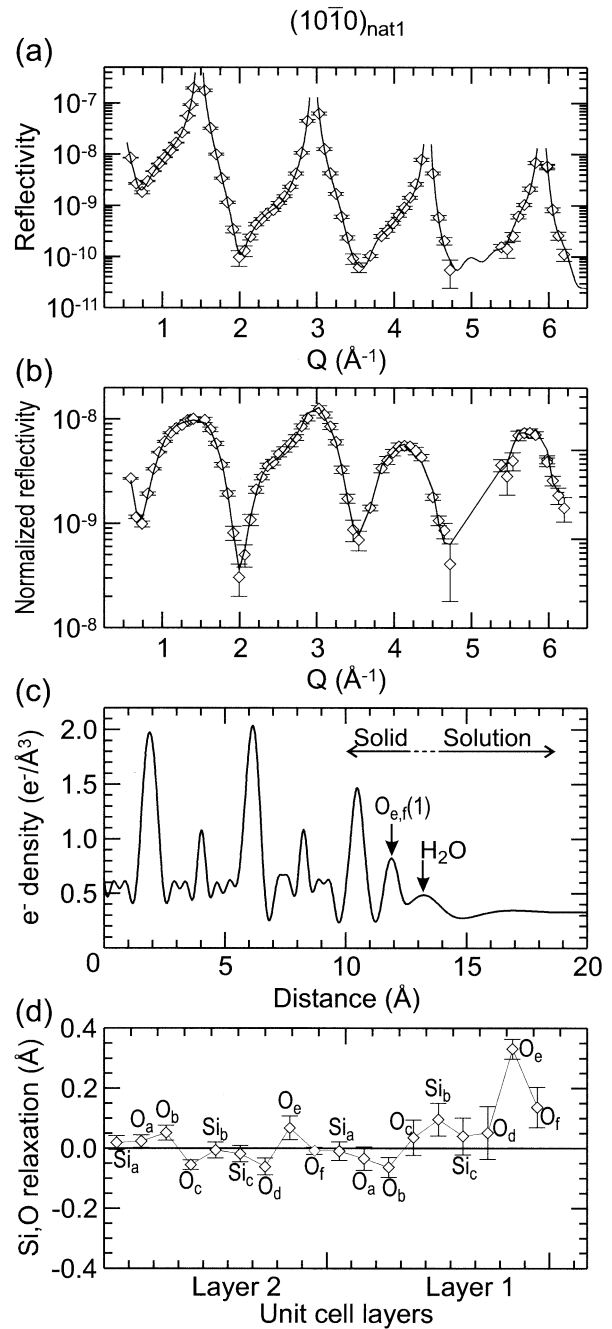
Fig. 12. Best fit results for X-ray reflectivity data obtained for the $(10\bar{1}0)_{nat1}$ natural surface. (a) Reflectivity data R(Q) and best fit. (b) Normalized reflectivity data $R(Q)\cdot[Qsin(Qd_{10\bar{1}0}/2)]^2$ and best fit. (c) Laterally-averaged electron density profile; $O_{e,f}(1)$ indicates the $O_{e,f}$ atom in the surface layer. (d) Relaxation parameters as a function of the unit cell layer. Positive and negative relaxations are toward the solution and the bulk crystal, respectively.

$\pm$ 0.4 molecules/26.57 Å^2 located at 2.4 $\pm$ 0.4 and 1.2 $\pm$ 0.2 Å beyond the hydroxyl groups of terminations α and β. Finally, while a reasonable electron density profile is obtained (Fig. 12c), rather high outward relaxation values are obtained for the most external oxygens (Fig. 12d), consistent with the qualitative assessment above. The surface roughness value obtained from the best fit (3.6 $\pm$ 0.3 Å) compares well with values obtained on $(10\bar{1}0)_{ann}$ and $(10\bar{1}0)_{nat2}$.

5. DISCUSSION

5.1. Impact of Annealing on the Structure of $(10\bar{1}0)$ and $(10\bar{1}1)$ Surfaces

X-ray reflectivity data collected on natural $(10\bar{1}0)$ and $(10\bar{1}1)$ growth surfaces of quartz are consistent with minor relaxation

of the mineral structure at the solid-water interface. No evidence for the presence of highly disturbed or amorphous silica layers was obtained, and extensive coverage of the quartz surface by such a coating can be ruled out. Indeed, care was taken in the present study to preserve the surface structure of the natural quartz samples, except for annealing. Severe chemomechanical treatment of the surfaces was avoided, because these preparation methods are known to result in fracturing and amorphization over a depth of several nm (Gratz et al., 1990; Noge et al., 1997). Furthermore, little or no structural difference was observed between annealed and natural surfaces of the same orientations, as surface 3c groups predominate in all but the $(10\bar{1}0)_{nat1}$ sample. This result agrees with previous LEED observations of the absence of reconstruction for quartz surfaces either chemically etched in HF or annealed at temperatures $\leq 500°C$ (Bart et al., 1992) and with the predicted predominance of 3c groups on $(10\bar{1}0)$ surfaces (Koretsky et al., 1997). Indeed, extended surface reconstruction was proposed to occur only above 571°C, that is, the temperature of the quartz $\alpha \leftrightarrow$ quartz β transition (Bart and Gautier, 1994). Reflectivity observations do not preclude possible healing of point or linear defects, as X-ray reflectivity is affected only by laterally-averaged electron density.

The predominance of surface 3c groups over 2c groups suggests that surface groups with a lower number of crystal bonds dissolve (or are incorporated at growth steps) more rapidly, as predicted previously from theoretical considerations (Lasaga, 1990; Gratz et al., 1991; Gratz and Bird, 1993b). Because of this greater reactivity, stable crystal surfaces such as $(10\bar{1}0)$ and $(10\bar{1}1)$ quartz faces should expose a minimal number of 2c groups, mostly at steps or as diffusion intermediates (adatoms) bonded to 3c groups (Gratz and Bird, 1993a). Our observations seem to confirm this assumption, except for the X-ray reflectivity results of $(10\bar{1}0)_{nat1,}$ which suggest that 2c groups cover 33% of the surface (assuming the absence of a contaminant molecule). While we cannot determine uniquely that this particular surface has a different termination, we can place constraints on this interpretation. For example, only steps of unit-cell height were observed on AFM images of $(10\bar{1}0)_{nat1}$, suggesting that only one surface termination was present on this sample. This is fully consistent with the lack of any systematic broadening of the rocking curve widths (e.g., Fig. 4) as a function of Q (not shown) beyond our experimental resolution. Because broadening of the rocking curve as a function of Q is sensitive to both the lateral step spacing and the step height (Fenter et al., 2001), our results imply that the typical surface domain size, as measured by X-ray reflectivity, is large with respect to the lateral resolution, consistent with the broad flat terraces visible in the AFM images in Fig. 3. Therefore, the strong changes in X-ray reflectivity for the $(10\bar{1}0)_{nat1}$ sample must be interpreted as a uniform termination of the surface, since multiple terminations having lateral domain sizes beyond the instrumental resolution would add incoherently and not produce the strong decrease in reflectivity observed for this surface. The simplest explanation for this observation is that the $(10\bar{1}0)_{nat1}$ surface contained a partial layer of 2c groups randomly distributed over 33% of the underlying β-terminated layer. Since we have not made any direct measurements of the elemental composition of the surface, we cannot rule out the possibility that this layer is due to the adsorption of some
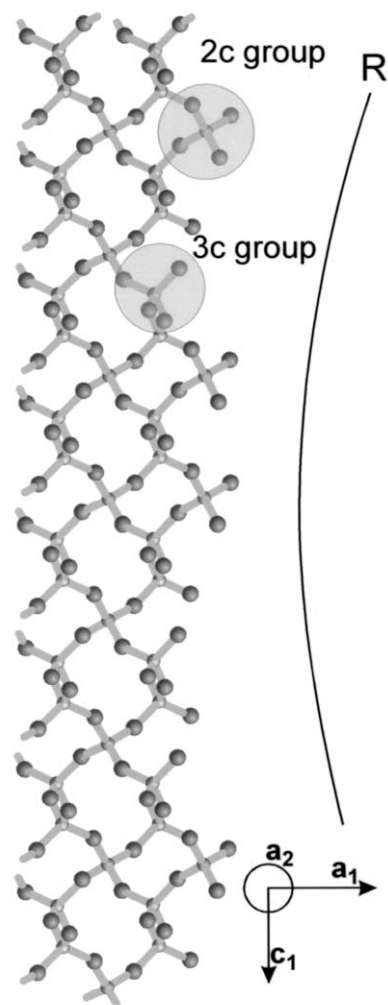

Fig. 13. Possible structure of $(10\bar{1}0)_{nat1}$ surface explaining X-ray reflectivity and AFM data. About 33% of the surface is covered by silica forming two crystal bonds with two other bulk tetrahedral units (2c groups); the remaining surface contains silica groups forming three crystal bonds (3c groups). The arc R visualizes the curvature of the AFM tip of nominal radius ~ 10 nm.

"contaminant." However, given the high uniformity that we have observed with the other growth surfaces, this appears unlikely. This distribution of surface groups would be seen by AFM as one termination with a small-scale roughness (Fig. 13).

5.2. Step Structure and Implications for Dissolution Reactions

Flat surfaces are believed to dissolve or grow mostly by subtraction or addition of growth units at steps (Burton et al., 1951). In this model, the mechanisms of dissolution and growth, and the possible incorporation of impurities, depend strongly on the structure and reactivity of the steps. AFM images and X-ray reflectivity data can provide some useful insight on this structure. AFM images revealed that steps on $(10\bar{1}1)$ and $(10\bar{1}0)$ surfaces have orientations corresponding to intersections between major growth planes, e.g., $[\bar{2}\bar{3}2]$ orienta-
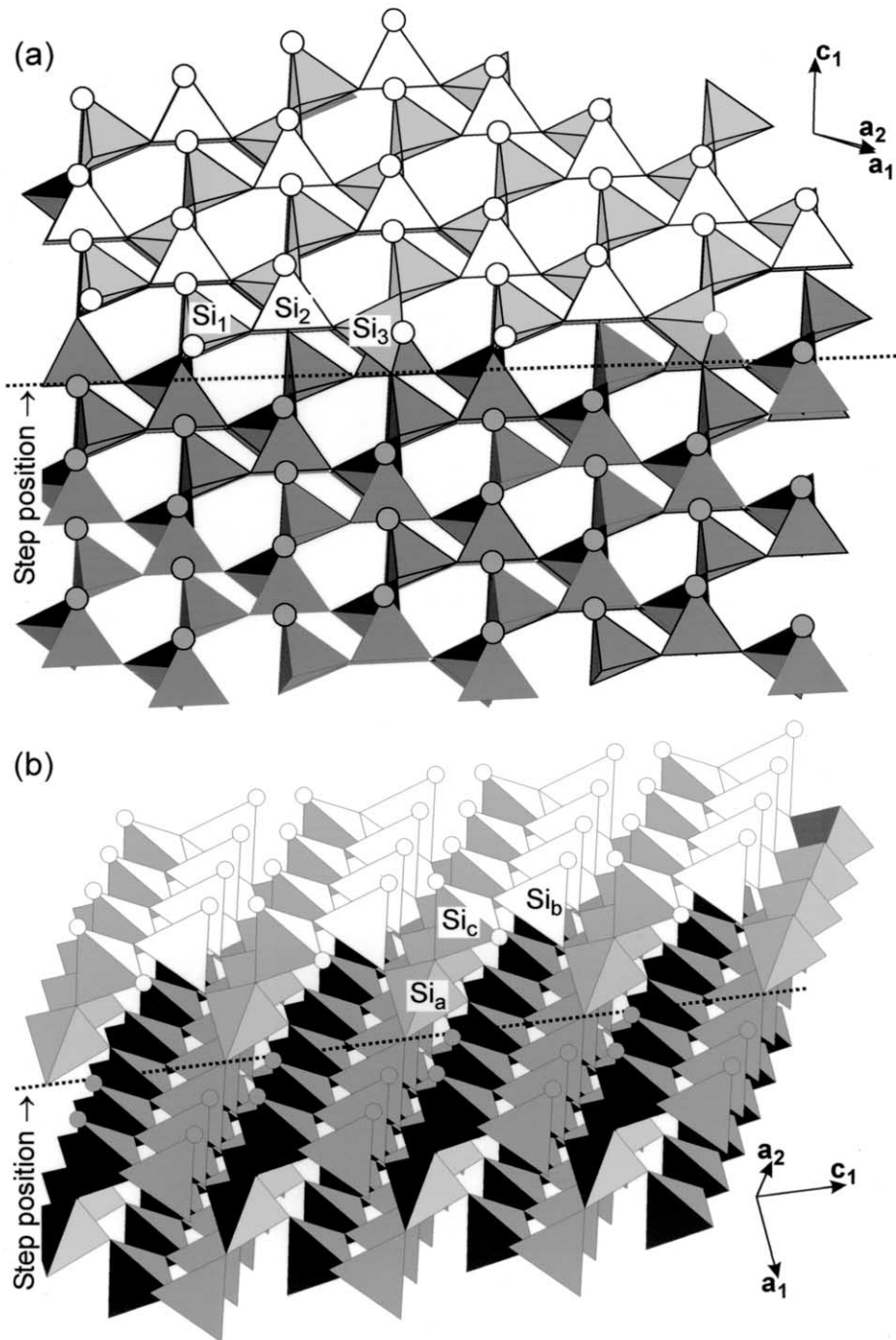
Fig. 14. Possible step structures on $(10\bar{1}1)$ and $(10\bar{1}0)$ surfaces. Silanol groups of the lower levels are represented as grey spheres, and those of the upper level as white spheres. (a) $[\bar{2}\bar{3}\,2]$ steps on $(10\bar{1}1)$ surfaces. (b) [001] steps on $(10\bar{1}0)$ surfaces.

tions for $(10\bar{1}1)$ surfaces, and $[0\bar{1}1]$ and [001] for $(10\bar{1}0)$ surfaces. Knowing the step orientations from AFM and the structure of terraces from X-ray reflectivity, the step atomic structure may be modeled by intersecting the unit-cell high terraces with vertical planes. Figure 14a shows that only surface Si_1 form 2c groups at the $[\bar{2}\bar{3}2]$ edges of $(10\bar{1}1)$ surfaces. Reconstitution of the [001] steps on $(10\bar{1}0)$ faces also points to

a stable framework, as all Si_a are fully coordinated to structural silica tetrahedral, while Si_b and Si_c groups expose only one and two free Si-O bonds, respectively (Fig. 14b). It is possible that step-exposed and terrace-exposed Si may not differ too much in terms of stability, and the possible presence of step-exposed 3c groups has to be taken into account for reliable estimation of dissolution/growth sites on quartz.

5.3. Surface Structure of Water

A layer of adsorbed water is consistent with electron density profiles on all probed surfaces. This layer is presumably retained at the surface via hydrogen bridges between silanol groups and oxygens of water molecules, and therefore is thought to be structured surface water. Etzler and Fagundus (1987) postulated that interfacial structuring of water would result in a decrease of the water density close to the silica surface. They modeled this decrease from a series of measurements on silica gels with decreasing pore size, and their model suggests that the density of water at ~1.7 Å from the surface should equal 0.93 times that of bulk water. Assuming a volume of ~30.3 Å^3 per molecule for bulk water, the adsorbed water layer is expected to contain either 2.8 molecules/26.57 Å^2 for ($10\bar{1}0$) surfaces, or 3.5 molecules/33.80 Å^2 for ($10\bar{1}1$) surfaces. For all but sample ($10\bar{1}0$)$_{nat1}$, the experimental water density is equal to or lower than these predicted values, confirming the hypothesis of Ezler and Fagundus (1987). We find that the number of adsorbed water molecules is consistent with the number of silanol groups per unit cell (excepting the ($10\bar{1}0$)$_{nat1}$ sample), suggesting that the driving force for the formation of this layer is likely the hydrogen bonding of these water molecules to surface silanol groups. These observations agree with those of previous studies of the calcite and barite surfaces (Fenter et al., 2000a; 2001) in which the number of adsorbed water molecules corresponded to the number of reactive sites on the mineral surface, and as found here, was substantially lower than the corresponding density of a densely packed layer of water molecules. However, the amount of adsorbed water in the first layer for ($10\bar{1}0$)$_{nat1}$ (2.8 ± 0.4 molecules/26.57 Å^2) is equal to the layer density of bulk water (~ 2.8 water/26.57 Å^2), and the fit becomes worse if the density of water is decreased. The amount of adsorbed water is also on average twice as high as that on the ($10\bar{1}0$)$_{nat2}$ and ($10\bar{1}0$)$_{ann}$ surfaces. This suggests that adsorbed water is somewhat more disordered at the ($10\bar{1}0$)$_{nat1}$ surface, in agreement with a surface model of terraces containing isolated silicon groups that are randomly distributed.

Structural organization of water on atomically flat surfaces may be expected to result in oscillations of water density within the interfacial solution through the so-called "hard-wall" effect (Cheng et al., 2001). Based on ab initio calculations, such density oscillations may be present at the quartz-water interface (Lasaga, 1990). In contrast, electrostatic considerations indicate that little or no water structuring occurs at the quartz surface (Sverjensky, 2001). Sum-frequency generation (SFG) studies of water-"fused quartz" (i.e., pyrolyzed silica) surfaces pointed to an absence of orientational ordering of water at near-neutral pH (Du et al., 1994). Our observation of only one layer of structurally modified water directly in contact with the surface agrees with the SFG results. This absence of extensive structuring at near-neutral pH was explained by competing effects of hydrogen bridging and net negative surface charge on the orientation of the water dipole (Du et al., 1994). This competition would lead to structural disorder in bulk water near the interface, which is consistent with our results.

5.4. Comparison of Smooth and Rough Quartz Surfaces

Because of their nearly "perfect" nature, and the precautions taken to avoid preparation artifacts, the Herkimer diamond surfaces may differ from ground quartz powder commonly used in solution chemistry studies. Quartz grains in surficial environments can expose surfaces without obvious crystallographic orientations (Gratz and Bird, 1993a; Koretsky et al., 1998; Schulz and White, 1999). Yet, Bloss and Gibbs (1963) showed that conchoidally fractured surfaces are composed of submicroscopic combinations of preferred cleavage planes, e.g., $\{10\bar{1}1\}$, $\{01\bar{1}1\}$, $\{11\bar{2}2\}$, and less pronounced cleavages on $\{0001\}$, $\{11\bar{2}1\}$, $\{51\bar{6}1\}$ and $\{10\bar{1}0\}$. Exposed silica groups on these irregular surfaces should have various numbers of crystal bonds with bulk silica groups, and consequently varying degrees of reactivity in solution (Gratz et al., 1991; Gratz and Bird, 1993b). In contrast, most surface silica groups on basal terraces of $\{10\bar{1}0\}$ and $\{10\bar{1}1\}$ crystal faces are 3c groups, and therefore would have relatively low reactivity. However, Gratz and Bird (1993b) demonstrated that the same rate law could be applied to describe the dissolution properties of quartz powder and crystal faces by adjusting only one proportionality constant. This observation suggests that similar energetics govern the dissolution reactions in both cases, and therefore our conclusions obtained on "perfect" crystal faces may apply as well to other quartz surfaces.

5.5. Influence of Trace Components on the Modeled Interface Structure

Modeling of the interface structure was performed assuming that the interface was composed dominantly of bulk and surface silicon and oxygen atoms in the solid quartz and water in the solution. The presence of trace elements in the bulk quartz or low concentrations of other dissolved components in the water would not have altered the laterally-averaged electron densities of layers parallel to the interface within the uncertainty of the model fits. However, the possible occurrence of two additional solution components should be discussed in more detail. The first is dissolved silica which, if present in high concentrations, may adsorb as an incomplete monolayer on the quartz surface (Holt and King, 1955). All quartz surfaces stored in water and then analyzed by AFM or X-ray reflectivity were washed extensively with deionized SiO$_2$-free water before the measurement. Adsorbed silica desorbs in SiO$_2$-free basic or near-neutral solutions within hours (Holt and King, 1955), and therefore the quartz surfaces were probably free of adsorbed silica. The second type of solute includes the organic solvents methanol and acetone. Only high-purity solvents were used to clean the quartz surfaces, and the final cleaning step was always in deionized water in the ultrasonicator, which would have solubilized and removed the majority of the organic molecules (Goss, 1992). Some of the "dust" observed in AFM images may be organic residues. However this "dust" was not extensive enough to mask unit-cell-high steps in the images and effectively could be ignored in modeling the reflectivity data.

6. CONCLUSIONS

Structural and morphologic characterization of natural quartz growth faces was performed by AFM and X-ray reflectivity with minimal preparation of the surfaces. Results indicate that little or no amorphous silica is present, the surface is likely fully hydroxylated, and only minor relaxations (< 0.4 Å) have

occurred close to the surface (≤ 14 Å). They further indicate that no structuring of the near-surface water is observed beyond the first layer of adsorbed water molecules. Finally, most surface silicon tetrahedra form three bonds with the bulk tetrahedral units, thereby reducing the steric freedom and chemical reactivity of surface silica groups.

X-ray reflectivity measurements demonstrate that rigorous structural models for surfaces can be constructed to support molecular mechanisms for mineral dissolution and growth. Such knowledge should be useful for understanding the mechanism of impurity incorporation during quartz growth, which is important for economic production of high-quality crystals for piezoelectric and oscillator applications. Structural models of nearly-perfect surfaces and experiments performed on such surfaces may also help understand the reactivity of powdered quartz in experimental studies and of fine-grained weathered quartz in natural systems.

Associate editor: P. A. Maurice

REFERENCES

Bart F. and Gautier M. (1994) A LEED study of the (0001) α-quartz surface reconstruction. *Surf. Sci.* **311,** L671–L676.

Bart F., Gautier M., Duraud J. P., and Henriot M. (1992) (01$\bar{1}$0) α-quartz surface: a LEED, XANES and ELS study. *Surf. Sci.* **274,** 317–328.

Bart F., Gautier M., Follet F., and Duraud J. P. (1994) Electronic structure of the (0001) and (10$\bar{1}$0) quartz surfaces and their defects as observed by reflection electron energy loss spectroscopy (REELS). *Surf. Sci.* **306,** 342–358.

Berger G., Cadore E., Schott J., and Dove P. M. (1994) Dissolution rate of quartz in lead and sodium solutions between 25 and 300°C: effect of the nature of surface complexes and reaction affinity. *Geochim. Cosmochim. Acta* **58,** 541–551.

Bloss F. D. and Gibbs G. V. (1963) Cleavage in quartz. *Am. Miner.* **48,** 821–838.

Boisen M. B. and Gibbs G. V. (1990) Mathematical crystallography. *Rev. Mineral.* **15,** Mineralogical Society of America, Washington, DC.

Brady P. V. and Walther J. V. (1989) Controls on silicate dissolution in neutral and basic pH solutions at 25°C. *Geochim. Cosmochim. Acta.* **53,** 2823–2830.

Brady P. V. and Walther J. V. (1990) Kinetics of quartz dissolution at low temperatures. *Chem. Geol.* **82,** 253–264.

Brantley S. L., Crane S. R., Crerar D. A., Hellmann R., and Stallard R. (1986) Dissolution at dislocation etch pits in quartz. *Geochim. Cosmochim. Acta.* **50,** 2349–2361.

Brown I. D. (1992) Chemical and steric constraints in inorganic solids. Acta Cryst. **B48,** 553–572.

Burton W. K., Cabrera N., and Frank F. C. (1951) The growth of crystals and the equilibrium structure of their surfaces. *Phil. Trans. Roy. Soc. Lond.* **A243,** 299–358.

Cheng L., Fenter P., Nagy K. L., Schlegel M. L., and Sturchio N. C. (2001) Molecular-scale density oscillations in water adjacent to a mica surface. *Phys. Rev. Lett.* **87,** 15610–15613.

Coston J. A., Fuller C. C., and Davis J. A. (1995) Pb^{2+} and Zn^{2+} adsorption by a natural aluminum- and iron-bearing surface coating on an aquifer sand. *Geochim. Cosmochim. Acta.* **59,** 3535–3547.

Davies S. N. and De Wiest R. C. M. (1966) *Hydrogeology.* John Wiley and Sons, New York.

Davis J. A., Coston J. A., Kent D. B., and Fuller C. C. (1998) Application of the surface complexation concept to complex mineral assemblages. *Env. Sci. Tech.* **32,** 2820–2828.

De Leeuw N. H., Higgins F. M., and Parker S. C. (1999) Modelling the surface structure and stability of α-quartz. *J. Phys. Chem. B.* **103,** 1270–1277.

Dove P. M. (1994) The dissolution kinetics of quartz in sodium-chloride solutions at 25°C to 300°C. *Am. J. Sci.* **294,** 665–712.

Dove P. M. (1995) Kinetic and thermodynamic controls on silica reactivity in weathering environments. In *Chemical weathering rates of silicate minerals.* (eds. A. F. White and S. L. Brantley). Mineralogical Society of America, Washington, DC, pp. 235–290.

Dove P. M. and Crerar D. A. (1990) Kinetics of quartz dissolution in electrolyte solutions using a hydrothermal mixed flow reactor. *Geochim. Cosmochim. Acta.* **54,** 955–969.

Dove P. M. and Elston S. F. (1992) Dissolution kinetics of quartz in sodium chloride solutions: analysis of existing data and a rate model for 25°C. *Geochim. Cosmochim. Acta.* **56,** 4147–4156.

Dove P. M. and Nix C. J. (1997) The influence of the alkaline earth cations, magnesium, calcium, and barium on the dissolution kinetics of quartz. *Geochim. Cosmochim. Acta.* **61,** 3329–3340.

Du Q., Freysz E., and Shen Y. R. (1994) Vibrational spectra of water molecules at the quartz/water interface. *Phys. Rev. Lett.* **72,** 238–241.

Eng P. J., Trainor T. P., Brown, Jr. G. E., Waychunas G. A., Newville M., Sutton S. R., and Rivers M. L. (2001) Structure of the hydrated α-Al_2O_3(0001) surface. *Science.* **288,** 1029–1033.

Etzler F. M. and Fagundus D. M. (1987) The extent of vicinal water. Implications from the density of water in silica pores. *J. Colloid Interface Sci.* **115,** 513–519.

Feidenhans'l R. (1989) Surface structure determination by X-ray diffraction. *Surf. Sci. Rep.* **10,** 105–188.

Fenter P. and Sturchio N. C. (1999) Structure and growth of stearate monolayers on calcite: first results of an in situ x-ray reflectivity study. *Geochim. Cosmochim. Acta.* **63,** 3145–3152.

Fenter P., McBride M. T., Srajer G., Sturchio N. C., and Bosbach D. (2001) Structure of barite (001)- and (210)-water interfaces. *J. Phys. Chem. B.* **105,** 8112–8119.

Fenter P., Geissbühler P., DiMasi E., Srajer G., Sorensen L., and Sturchio N. C. (2000a) Surface speciation of calcite observed in situ by high-resolution X-ray reflectivity. *Geochim. Cosmochim. Acta.* **64,** 1221–1228.

Fenter P., Teng H., Geissbühler P., Hanchar J. M., Nagy K. L., and Sturchio N. C. (2000b) Atomic-scale structure of the orthoclase(001)-water interface measured with high-resolution X-ray reflectivity. *Geochim. Cosmochim. Acta.* **64,** 3663–3673.

Gallei E. and Parks G. A. (1972) Evidence for surface hydroxyl groups in attenuated total reflectance spectra of crystalline quartz. *J. Colloid Interface Sci.* **38,** 650–651.

Gautier J. -M., Oelkers E. H., and Schott J. (2001) Are quartz dissolution rates proportional to B.E.T. surface areas? *Geochim. Cosmochim. Acta.* **65,** 1059–1070.

Geerlings P., Tyariel N., Botrel A., Lissillour R., and Mortier W. J. (1984) Interaction of surface hydroxyls with adsorbed molecules. A quantum-chemical study. *J. Phys. Chem.* **88,** 5752–5759.

Giacovazzo C. (1992) Crystallographic Computing. *Fundamentals of Crystallography.* In: (ed. C. Giacovazzo). International Union of Crystallography, Oxford University Press, pp. 141–228.

Goss K. U. (1992) Effects of temperature and relative humidity on the sorption of organic vapors on quartz sand. *Env. Sci. Tech.* **26,** 2287–2294.

Gratz A. J. and Bird P. (1993a) Quartz dissolution: theory of rough and smooth surfaces. *Geochim. Cosmochim. Acta* **57,** 977–989.

Gratz A. J. and Bird P. (1993b) Quartz dissolution: negative crystal experiments and a rate law. *Geochim. Cosmochim. Acta* **57,** 965–976.

Gratz A. J., Bird P., and Quiro G. B. (1990) Dissolution of quartz in aqueous basic solution, 106-236°C: surface kinetics of "perfect" crystallographic faces. *Geochim. Cosmochim. Acta* **54,** 2911–2922.

Gratz A. J., Manne S., and Hansma P. K. (1991) Atomic force microscopy of atomic scale ledges and etch pits formed during dissolution of quartz. *Science* **251**, 1343–1346.

Heaney P. J. (1996) Structure and chemistry of the low-pressure silica polymorphs. In *Silica*. (eds. P. J. Heaney, C. T. Prewitt, and G. V. Gibbs). Mineralogical Society of America, Washington, DC, pp. 1–40.

Heggie M. and Jones R. (1987) Density functional-analysis of the hydrolysis of Si-O bonds in disiloxane—application to hydrolytic weakening in quartz. *Phil. Mag. Lett.* **55**, 47–51.

Henderson J. H., Syier J. K., and Jackson M. L. (1970) Quartz dissolution as influenced by pH and the presence of a disturbed surface layer. *Israel. J. Chem.* **8**, 357–372.

Hiemstra T. and Van Riemsdijk W. H. (1990) Multisite activated complex dissolution of metal hydroxides: a thermodynamic approach applied to quartz. *J. Colloid Interface Sci.* **136**, 132–150.

Hiemstra T., Venema P., and Van Riemsdijk W. H. (1996) Intrinsic proton affinity of reactive surface groups of metal (Hydr)oxides: the bond valence principle. *J. Colloid Interface Sci.* **184**, 680–692.

Holt P. F. and King D. T. (1955) The chemistry of silica surfaces. *J. Chem. Soc. Lond.* 773–779.

Kamiya H. and Shimokata K. (1976) The role of salts in the dissolution of powdered quartz. In *Proceedings of international symposium on water-rock interactions*. (eds. J. Cadek and T. Paces). Czechoslovakian Geological Survey, Prague, pp 426–429.

Kihara K. (1990) An X-ray study of the temperature dependence of the quartz structure. *Eur. J. Mineral.* **2**, 63–77.

Knauss K. G. and Wolery T. J. (1988) The dissolution kinetics of quartz as a function of pH and time at 70°C. *Geochim. Cosmochim. Acta.* **52**, 43–53.

Koretsky C. M., Sverjensky D. A., and Sahai N. (1998) A model of surface site types on oxide and silicate minerals based on crystal chemistry: implication for site types and density, multi-site adsorption, surface infrared spectroscopy, and dissolution kinetics. *Am. J. Sci.* **298**, 349–438.

Koretsky C. M., Sverjensky D. A., Salisbury J. W., and D'aria D. M. (1997) Detection of surface hydroxyl species on quartz, γ-alumina, and feldspars using diffuse reflectance infrared spectroscopy. *Geochim. Cosmochim. Acta* **61**, 2193–2210.

Koudriachova M. V., Beckers J. V. L., and De Leeuw S. W. (2001) Computer simulation of the quartz surface: a combined ab initio and empirical potential approach. *Comp. Mat. Sci.* **20**, 381–386.

Kubicki J. D., Xiao Y., and Lasaga A. C. (1993) Theoretical reaction pathways for the formation of $[Si(OH)_5]^{1-}$ and the deprotonation of orthosilicic acid in basic solution. *Geochim. Cosmochim. Acta* **57**, 3847–3853.

Lasaga A. C. (1990) Atomic treatment of mineral-water surface reactions. In *Mineral-water interface geochemistry*. (eds. M. F. Hochella, Jr. and A. F. White). Mineralogical Society of America, Washington, DC, pp. 17–85.

Lasaga A. C. and Gibbs G. V. (1990) Ab initio quantum mechanical calculations of surface reactions—a new era? In *Aquatic chemical kinetics*. In: (ed. W. Stumm). Wiley Interscience, New York, pp. 259–289.

MacDonald R. (1983) Silicon in igneous and metamorphic rocks. In *Silicon geochemistry and biogeochemistry*. (ed. S. R. Aston). Academic Press, New York, pp. 1–37.

Manceau A., Schlegel M. L., Nagy K. L., and Charlet L. (1999) Evidence for the formation of trioctahedral clay upon sorption of Co^{2+} on quartz. *J. Colloid Interface Sci.* **220**, 181–197.

Morris R. C. and Fletcher A. B. (1987) Increased solubility of quartz following ferrous-ferric iron reactions. *Nature* **330**, 558–561.

Morrow B. A. and Cody A. (1976) Infrared studies of reactions on oxide surfaces. 6. Active sites on dehydroxylated silica for the chemisorption of ammonia and water. *J. Phys. Chem.* **80**, 1998–2004.

Munkholm A., Brennan S., and Carr E. C. (1997) A comparison of surface roughness as measured by atomic force microscopy and X-ray scattering. *J. Appl. Phys.* **82**, 2944–2953.

Noge S., Araki N., Komine K., Susuki H., Shiraishi H., and HohKawa K. (1997) Study of the microscopic surface structure of a quartz substrate for surface acoustic wave devices. *Jap. J. Appl. Phys.* **36**, 3081–3086.

O'Day P. A., Chisholm-Brause C. J., Towle S. N., Parks G. A., and Brown Jr. G. E. (1996) X-ray absorption spectroscopy of Co(II) sorption complexes on quartz (α-SiO_2) and rutile (TiO_2). *Geochim. Cosmochim. Acta* **60**, 2515–2532.

Rimstidt J. D. (1997) Quartz solubility at low temperatures. *Geochim. Cosmochim. Acta* **61**, 2553–2558.

Rimstidt J. D. and Barnes H. L. (1980) The kinetics of silica-water reactions. *Geochim. Cosmochim. Acta* **44**, 1683–1699.

Robinson I. K. (1986) Crystal truncation rods and surface roughness. *Phys. Rev. B.* **33**, 3830–3836.

Robinson I. K. and Tweet D. J. (1992) Surface X-ray Diffraction. *Rep. Prog. Phys.* **55**, 599–651.

Rossman G. R. (1994) Colored varieties of the silica minerals. In *Silica*. (eds. P. J. Heaney, C. T. Prewitt, and G. V. Gibbs). Mineralogical Society of America, Washington, DC, pp. 433–467.

Schulz M. S. and White A. F. (1999) Chemical weathering in a tropical watershed, Luquillo mountains, Puerto Rico III: Quartz dissolution rates. *Geochim. Cosmochim. Acta* **63**, 337–350.

Schwarzentruber J., Furst W., and Renon H. (1987) Dissolution of quartz into dilute alkaline solutions at 90°C: a kinetic study. *Geochim. Cosmochim. Acta* **51**, 1867–1874.

Simpson G. J., Sedin D. L., and Rowlen K. L. (1999) Surface roughness by contact versus tapping mode atomic force microscopy. *Langmuir* **15**, 1429–1434.

Sturchio N. C., Chiarello R. P., Cheng L. W., Lyman P. F., Bedzyk M. J., Qian Y. L., You H. D., Yee D., Geissbuhler P., Sorensen L. B., Liang Y., and Baer D. R. (1997) Lead adsorption at the calcite-water interface: Synchrotron X-ray standing wave and X-ray reflectivity studies. *Geochim. Cosmochim. Acta* **61**, 251–263.

Sverjensky D. A. (2001) Interpretation and prediction of triple layer model capacitances and the structure of the oxide-electrolyte-water interface. *Geochim. Cosmochim. Acta* **65**, 3643–3655.

Tester J. W., Worley W. G., Robinson B. A., Grigsby C. O., and Feerer J. L. (1994) Correlating quartz dissolution kinetics in pure water from 25°C to 625°C. *Geochim. Cosmochim. Acta* **58**, 2407–2420.

Ugliendo P., Saunders V., and Garrone E. (1990) Silanol as a model for the free hydroxyl of amorphous silica: ab initio calculations of the interaction. *J. Phys. Chem.* **94**, 2260–2267.

Xiao Y. and Lasaga A. C. (1996) Ab initio quantum mechanical studies of the kinetics and mechanisms of silicate dissolution: OH^- catalysis. *Geochim. Cosmochim. Acta* **60**, 2283–2295.